———————

TIME-VARYING POWER-SERIES ANALYSIS IN THE DESIGN OF μ-WAVE HIGHLY-LINEAR GaN ACTIVE MIXERS AND PAs

Candidate
Lorenzo Pagnini

Supervisor
Prof. Alessandro Cidronali

PhD Coordinator
Prof. Fabio Shoen

———————

Università degli Studi di Firenze, Dipartimento di Ingegneria dell'Informazione (DINFO).

Alla mia famiglia

Acknowledgments

Contents

Chapter 1

Introduction

1.1 Motivations

It is a matter of fact that Gallium Nitride (GaN) High Electron Mobility Transistor (HEMT) technologies offer the advantage of an excellent trade-off between costs and high-frequency performance, in a high-volume device production process, compared to other wide-band-gap semiconductor technologies, like Silicon Carbide (SiC) [1] or GaN-on-SiC [2–4].

Recent literature reports developments of GaN for power amplifiers [5]–[6], oscillators [7], low-noise amplifiers (LNA) [8], and because of their excellent power handling, also passive circuits like resistive mixers [9]- [10], vector modulators [11], and even filters [12]. Because of their very high maximum operating temperature, namely $700°C$ versus $300°C$ for GaAs, GaN based devices have also been adopted for critical high temperature instrumentation circuits, [5], [13]. In this perspective, a linear front-end at micro-wave developments, [14], takes advantage of the inherent characteristic of wide-band gap semiconductors based devices, and in particular of GaN HEMTs, [15].

The GaN technology is considered to be suitable for the development of highly linear mixer, as witnessed by the recent literature, [16,17], which almost entirely considers the resistive mixer topology, and discusses their significantly high linearity properties. This feature is attributed to the GaN HEMT's breakdown voltage being higher than their GaAs counterparts and other high-speed device technologies, Fig. 1.1, which makes the un-biased device channel resistance only very weakly nonlinear across a wide voltage range.

Moving from this experimental evidence, the main idea behind this thesis work is the expectation that active mixers, namely the drain-pumped and the gate-pumped configurations, as well as supply-modulated power-amplifiers (SMPAs), take advantage of the GaN's wide drain-source I/V range in terms of linearity. The reasons leading to such considerations are explained below.

It is well known in the literature that the injection of a large local-oscillator power (PLO) benefits the mixers both for the conversion gain and the linearity performance [18–20]. In case the LO signal is injected at the device drain-side, i.e. in the drain-pumped configuration, the wide drain-source I/V range allows the application of a large PLO dynamic. Very few drain-pumped mixers were reported in literature, [21–28], none of which in GaN technology. In this thesis work, the first GaN-based drain-pumped mixer is reported, in which the positive impact of the technology on the linearity, as well as on the conversion gain, was experimentally proven.

In the gate-pumped configuration, the GaN-technology is expected to provide a double advantage. In addition to the high available-span also at the gate side, due to the GaN high breakdown-voltage of the gate-source junction, this configuration is expected to generate reduced intermodulation-products by itself. In fact, since in this case the drain-bias is in a region of flatness drain-source I/V characteristics, we expect a reduction in the inter-modulations related to the output conductance across a wide IF signal span. It is worth noting that the linearity property of the GaN-based gate-pumped mixer was already experimentally observed in [29], but without providing any explanation about it. In the present thesis work, the concept explained above was theoretically demonstrated by comparing the results of two independent analyzes; the one taking into account only the device transconductance, while the other considering the whole circuit model. These results laid the foundations for the development of a highly-linear GaN-based gate-pumped mixer for radar applications exhibiting a state-of-the-art input-referred third-order intercept-point (IIP3) figure-of-merit.

The expected benefits of the GaN technology don't concern only the mixers. In a similar manner, this technology is expected to open new frontiers of linearity also for power amplifiers (PAs), in particular for the class of SMPAs. In fact, in GaN SMPAs the magnitude of the drain signal has an available span such as to make it capable of influencing the overall distortion mechanism. In [30], a decrease in the third-order intermodulations power (IMP3) for a GaN SMPA was shown. In this thesis, the conditions for a

better inner-cancellation of the intermodulations were found, leading the overall linearity to a further improve. The linearity performance has been proven by the measurements carried out on a GaN-based SMPA developed for this purpose.
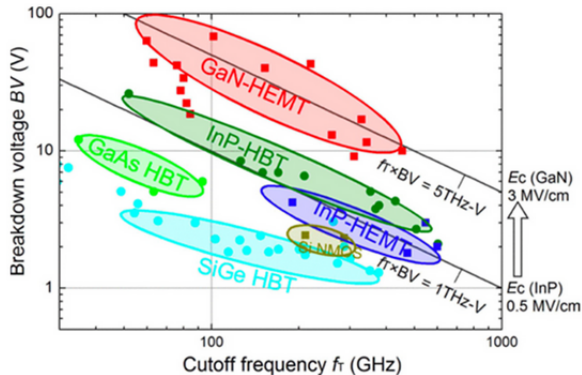
Figure 1.1: comparison of breakdown voltage and cut-off frequency among various high-speed device technologies (Keisuke Shinohara, IEEE Trans. on Electron Devices "Scaling of GaN HEMTs and Schottky Diodes for Submillimeter-Wave MMIC Applications")

1.2   Analysis method

In this scenario, a key role was played by a qualitative approach that characterized the analysis-stage of the circuits. This approach was inspired by the well-known time-varying Volterra-series analysis [31]. This analysis, based on the knowledge that the large signal, as the local-oscillator for a mixer, determines the main operation of the circuit, models the effect of such large signal as a time-varying modulation of the circuit components. As such, the time-domain waveforms of each component contain information regarding the global operation of the circuit. It is widely known that this approach is able to get very accurate predictions on field-effect transistors intermodulations, but at the cost of a considerable effort for the preliminary device parameters extraction [32].

In this thesis work, rather than extracting the waveforms of all the circuit components, we extracted the ones of the components which make the major

contribution to the overall circuit operation. This made the analysis easier to employ, and at the same time provides the design-stage with both a qualitative and an experimental aspect. Furthermore, since in this work the analysis purposes were not to make accurate predictions but rather to capture the main mechanisms governing the nonlinear-circuits operation, the frequency dependence was not considered. This made the time-varying Volterra-series analysis converge to the more simple time-varying power-series analysis.

The time-varying power-series analysis accompanied the whole thesis work and helped in different aspects in the design flow. The first application presented in this thesis concerns a drain-pumped mixer. In particular, the transconductance time-domain-waveform of a GaN-device allowed both to experimentally evaluate the impact of the technology on the mixer conversion gain (CG) and to find the mixer's optimum bias conditions. Concerning the gate-pumped configuration, the analysis was employed for three different purposes. Firstly, to prove the negligible contribution of the device drain-source conductance to the overall mixer operation. Then, to extrapolate the IIP3 figure-of-merit of a gate-pumped mixer from the experimental data of stand-alone-devices, thus enabling a straightforward comparison between different technologies. Finally, to provide the first analytical-based explanation for the phenomenon of the intermodulation-reduction when the PLO increases.

Furthermore, the use of the analysis has gone beyond the field of mixers. In fact, the effect of the drain-signal in a SMPA was approached as the one of the local-oscillator in a drain-pumped mixers. This enabled the experimental prediction of intermodulations cancellation occurring in SMPAs, as well as the identification of the responsible terms.

Finally, a case study concerning the application of the analysis on a GaAs-based quad-fet passive mixer is presented. In particular, the goal was to investigate the relation between the time-domain waveforms of the drain-source conductances and the RF-to-IF isolation provided by the mixer. The results of the analysis led to the design of a new architecture for the LO balun, and its positive impact on the RF-to-IF isolation was experimentally proven.

1.3 Thesis organization

The structure of the thesis was conceived with the purpose of highlighting the original scientific contributions. Therefore, the chapters reflect this choice, containing only material whose originality was recognized. Each initial page of each chapter contains a footnote specifying how the relative content contributed scientifically.

The organization of the thesis is as follows. In chapter 2 the first GaN-based drain-pumped mixer was introduced, and a comparison between active and passive GaN mixers, represented by the drain-pumped and the resistive configurations respectively, was carried out in an actual radar operating context. In chapter 3 the gate-pumped configuration was considered. The main nonlinear contributions to the overall operation of a GaN-based gate-pumped mixer were identified. A subsequent experimental-based comparison, in terms of linearity, between GaN and GaAs-based gate-pumped mixers was carried out. In chapter 4 a highly-linear gate-pumped mixer in GaN technology is presented, as well as the first analytical explanation concerning the dependence of the intermodulations on the PLO. In chapter 5 is shown how the GaN technology opens up new frontiers of linearity also for SMPAs. In such context, the SMPA operation was viewed as that of a drain-pumped mixer, by which the conditions for a drop in the intermodulations were predicted. Finally, in the appendix A an application of the time-varying power-series analysis in the context of high-RF-to-IF-isolation passive-mixers is reported.

Chapter 2

Active and passive GaN mixers in radar scenario

This chapter aims twofold; from the one side, it introduces the first drain-pumped (DP) mixer in Gallium Nitride (GaN) technology. From the other side, it reports an extensive comparison with the passive counterpart, namely the resistive mixer. Concerning the GaN DP mixer, a method aimed to predict the optimum bias conditions for active DP-mixers is described. This method leads to high conversion gain (CG) and linearity, along with the efficient use of the local oscillator drive level. A mixer prototype was designed and fabricated according to the discussed design principles; it exhibited a CG and an input third-order intercept point (IIP3) of $+10\,dB$ and $+11\,dBm$ respectively. Both the figures exceed the documented limitations for the class of mixers considered in this work. The prototype was also tested in a radar-like setup operating in the S-band frequency-modulated continuous-wave (FMCW) mode. For comparison purposes, a resistive mixer was designed and fabricated using the same GaN HEMT technology. [1]

---

[1]The part of this chapter included in the subsection "Preliminary DP Behavioral Analysis" was presented as "Analysis of a Single-Ended GaN-based Drain-Pumped Mixer for Radar Applications" at the *53rd Annual Meeting of the Associazione Società Italiana di Elettronica (SIE)* [33]. The rest of the chapter was published as "A GaN-HEMT Active Drain-Pumped Mixer for S-Band FMCW Radar Front-End Applications" in Sensors [34].

2.1   Introduction

In many modern microwave receiving systems, a high level of dynamic range
is a crucial feature, and a mixer is a functional block capable of influencing
the overall system performance from this point of view. In the literature, it
is well known that resistive mixers show the best performance in terms of
linearity [35]. Nevertheless, their linearity features further benefit from using
High Electron Mobility Transistors (HEMT) implemented in Gallium Nitride
(GaN) technology as highlighted in the recent literature [16, 17]; resistive
mixers suffer from frequency conversion losses. For this reason, a low-noise
amplifier (LNA) is introduced as first stage of the receiver chains, to com-
pensate the losses and the subsequent added noise. However, since modern
radar architectures make use of a large number of receivers and transmitter
modules [36, 37], the presence of the LNAs represents a significant increase in
the overall system cost and complexity [38]. This is even more stringent when
radar classification of UAV is of concern [39–41]. In addition, the realization
of a low-complexity reader for transponder units [42, 43] requires a highly
dynamic receiver with a low count of subsystems. Therefore, the alleviation
of their specifications is an open challenging topic.

   In view of recent results [44], the problems previously described could
be addressed by introducing GaN-based active mixer topologies that can
provide linearity as well as gain. These considerations lead the authors to
introduce an active DP mixer using GaN technology. In addition, the reduced
complexity of such a mixer topology is considered as a fundamental feature,
given the complexity in modern radar-system architectures.

   The gate-pumped configuration is undoubtedly one of the most investi-
gated among the active single-ended mixers. The latter has been proposed
in a wide range of applications such as wireless communications [45, 46],
high-temperature applications [47], and radar systems [29].

   With reference to the previous considerations and specifically referring
to radar applications, the use of the DP topology is expected to provide
some important benefits as explained in the following. The intrinsic RF-LO
separation, a typical feature for the resistive configuration, is very relevant for
radar applications given the adjacency between the RF and the LO signal frequencies.
At the same time, the DP mixer topology preserves the CG, which is typical
for the active configurations.

   A demonstration of characterization and modeling of GaN-based devices
in a mixer-like setup using the drain-driven HEMT was discussed in [48].

Concerning DP mixers specifically, very few were reported in the literature [21–27, 49–51], of which only five are single-ended [22, 25–27, 49].

In [26], it was clearly shown that there is an improvement of both the conversion gain (CG) and input third-order intercept point (IIP3) with respect to the increasing level of LO power in CMOS-based technology; nevertheless, the LO power dynamic was limited to 10 dBm.

Recently, an experimental-based analysis aimed at testing the impact of the GaN technology on the DP mixer was carried out [33]. In that work, the experimental data were firstly extracted from a packaged GaN-based device, and then elaborated to provide behavioral predictions about its operation as an ideal DP mixer. As expected, GaN technology allows to overcome the LO power level limitation of CMOS and other III–V semiconductor technologies, predicting an increase of both the mixer's CG and IIP3. In the present work, the same device was considered for the design and implementation of a DP mixer. The mixer was characterized with single-tone and multi-tone measurements inside the S-band. To the authors' best knowledge, this is the first DP mixer in this technology and the first DP mixer operating in the S-band. Among the DP mixers in single-ended topology, the present work reports both the highest CG and IIP3.

2.1.1   Optimum-Bias Methods for DP Mixers

In the literature, the problem of the optimum bias point in active mixers is well addressed for the gate-pumped topology, on which studies have also recently been carried out [52, 53], but only a few works consider the DP topology. Concerning the gate-side, the general rule for achieving CG in DP mixers is to bias the device beyond its threshold voltage, and in [24], a method capable of predicting the bias value for achieving the maximum CG was proposed. Concerning the drain-side, the general rule for achieving CG is to set the drain-bias of the device close to the knee-voltage of its output characteristics, while to maximize it, the first Fourier coefficient of the time-varying waveform $g_m(t)$ has to be maximized. In [26], the coefficient was extracted and analyzed, but since it was a passive DP-mixer, the drain-bias optimization was not conceived. In addition, the extraction was performed starting from an approximate model. In this work, we propose a method that extracts the first Fourier coefficient of $g_m(t)$ directly from the physical device and for any desired drain-bias value, thus allowing for an experimentally based prediction of the optimum bias for active DP-mixers.

The analysis is inspired by the time-varying Volterra-series analysis [18, 31, 54–56]. This analysis models the effect of the LO signal, which is the source of strongly nonlinear mechanisms, as a time-modulation of the device's intrinsic elements. As such, the time-domain waveforms of each component contain information regarding the global operation of the circuit. It is widely known that this approach is able to obtain very accurate predictions on field-effect transistors intermodulations, but at the cost of a considerable effort for the preliminary device parameter extraction [32].

In this work, rather than extracting the waveforms of all the circuit components, we extracted the ones of the components that provide the major contribution to the overall circuit operation. This made the analysis easier to be implemented, and at the same time, it provides the design stage with both qualitative and experimental insights. Recently, this approach resulted into a valuable tool for mixer behavioral predictions due to both its experimental basis and its simplicity [33, 44, 57, 58]. The analysis of the present work is an extension of the approach used in [33] since in that case the Fourier coefficients were extracted for a single bias value. With respect to the harmonic-balance algorithm, this method has the following two main advantages. The first is its capability to get deep inside the mixer's conversion mechanism, and the second is that it is based on experimental data, thus allowing to obtain pseudo-measurements already in the design stage of the mixer.

2.1.2   DP-Mixer in the Radar Context

Given the perspective of implementation in the context of radar systems, the mixer was then involved in a radar-like setup, and its operation was tested in the presence of an FMCW S-band signal. With the purpose of obtaining a term of comparison, a resistive mixer, which is often a part of the actual radar system front-end, was designed and fabricated using the same device. The mixers were compared while operating in the radar setup and in the same conditions of RF and LO signals. The adopted comparison criterion was the output IF signal-to-noise-ratio (SNR), of which the DP mixer showed the highest value, exceeding the passive counterpart by $3\,\mathrm{dB}$.

2.2   Analysis

2.2.1   Preliminary Behavioral Analysis of DP Mixers

In this section a preliminary DP analysis based on experimental data was carried out. As first, the experimental extraction procedure is described, and then the results were compared with the ones resulting from the model. An RF tone of frequency 50 MHz was injected at the gate-side while the power at the drain-side was measured for different V_D values. The transconductance was then derived for each V_D value from the ratio between the output current and the input voltage in the frequency domain, as described in [59]. Under the assumption of LO matching, the LO power at the port 2 of the circuit in Figure 2.2 is approximately the LO power at the device drain-side. Therefore, by finding the analytical function that best approximates the extracted $g_m(V_D)$ curve and by assuming a sinusoidal LO source, the $g_m(t)$ extraction is straightforward as reported in the Figure 2.1(b), from which the first Fourier coefficient was calculated. For each extracted curve, the algorithm was repeated as the P_{LO} changed.

   A DP mixer operating in S-band was designed and simulated by means of the commercial CAD ADS. The conceptual schematic shown in figure 2.2 was the first step of the design. Subsequently, the MOMENTUM software was used with the aim of designing and electromagnetically simulating the whole circuit layout. The S-parameters of the whole layout were then imported at the schematic level and used for the harmonic-balance simulations of the DP mixer.

   The results of both the analyzes are shown in figure 2.3. The $g_{m1}(V_D)$ was extracted for a gate-bias of -2.3 V, while in the transistor-model the gate-bias was set to -2.6 V since its input I/V curves was found to be shifted of 3 V with respect to the ones of the physical device. The time-domain waveform $g_{m1}(t)$ was extracted for a drain-bias of 3.7 V, and the transistor-model was set with this value.

   From the Fig. 2.3 we can appreciate that the $G_{m_{-1}}$ coefficient effectively governs the CG of the DP mixer. Both the experimental-based and the model-based analyzes predict the CG to increase linearly up to $P_{LO} \approx 20$ dBm, after which the rapidity of change increases for a narrow P_{LO} range and then stops. The harmonic-balance algorithm predicts the CG to reach 10 dB.

   These results provided us the motivations for the development of a GaN-
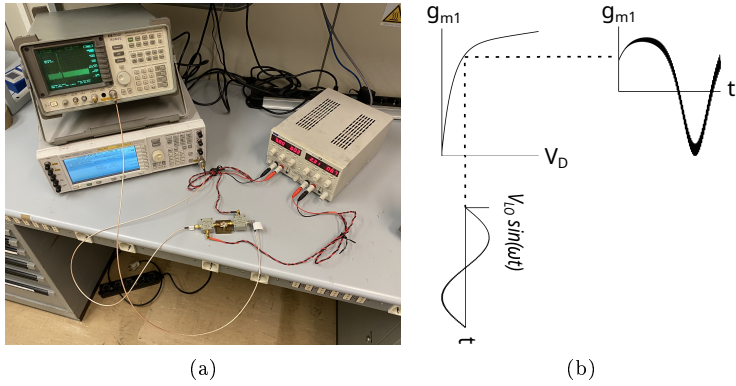
(a)   (b)

Figure 2.1: (a): the experimental setup for the $g_{m1}(V_D)$ extraction; (b): the extracted $g_{m1}(V_D)$ and the algorithm for the relative time-domain waveform extraction.
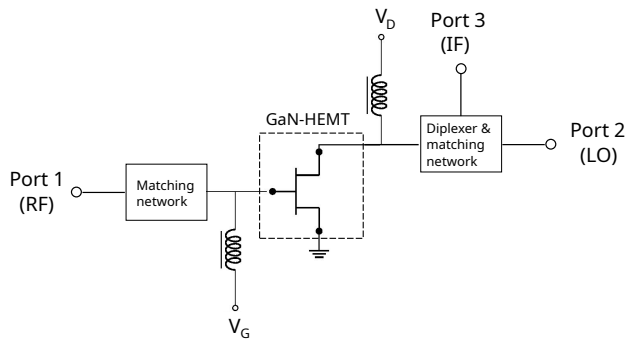

Figure 2.2: Schematic of the GaN-HEMT fundamental single-ended DP mixer.
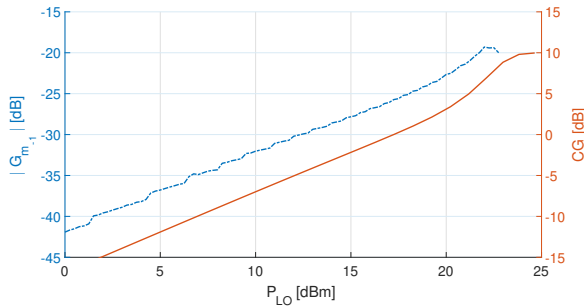
Figure 2.3: Comparison between the Fourier coefficient governing the CG of the DP mixer and the harmonic-balance simulated CG of the DP mixer.

based drain-pumped mixer. The data reported henceforth refer to the Wolfspeed's CGH40006S GaN HEMT [60]. However, the frequency-independent feature of the adopted approach makes it also suitable for devices operating at higher frequencies.

2.2.2 Existing Method for Prediction of Optimum Bias Point in DP Mixers

The bias optimization methods for DP mixers reported in the literature only concern the passive configuration. Since the drain-bias is fixed, the optimization only concerns the device's gate-side. As reported in the literature, the general rule for achieving CG is to bias beyond the device's threshold voltage in such a way as to have an appreciable transconductance value. In particular, as found in [23], there exists a bias value that maximizes the CG, and it is found by considering the curve g_m' as a function of V_D, where

$$g_m' = \frac{\partial g_m}{\partial V_D}.$$ (2.1)

After the extraction of $g_m'(V_D)$ for various V_G values as represented in Figure 2.4, the optimum V_G for passive DP mixers is the one corresponding to the highest curve for $V_D \approx +0.2\,\text{V}$, which for the considered device is $V_G = -2\,\text{V}$.

Figure 2.4: Simulated g'_m as a function of V_D for different values of V_G.

2.2.3 Proposed Method for Prediction of Optimum Bias Point in DP Mixers

Gate-Side

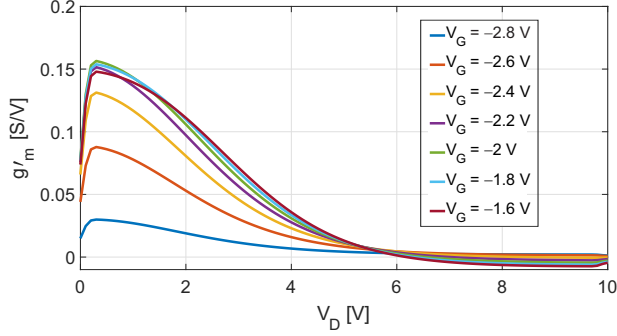Despite it was derived in the case of a passive DP mixer and its employment only concerns such devices [24, 50, 51], the validity of the method reported above can be extended to active DP mixers but with some adjustments. Firstly, the $g'_m(V_D)$ is extracted for V_D beyond the device's knee voltage; for the device considered in this work, the knee voltage encompasses the region of $+1 < V_D < +5$ V. By looking at Figure 2.4, the existing method would consider the curve at $V_G = -1.6$ V as the proper gate-bias since it is the highest in the V_D range belonging to the knee region. However, such bias value would shift the knee voltage in the positive direction leading to a large LO dynamic for reaching the maximum CG. This is evident from Figure 2.5a, in which the device's output characteristics are reported. The second derivative of each $I_D(V_D)$ curve, multiplied by a proper scale factor k, was also reported to help the visualization of the knee region. In fact, $\partial^2 I_D/\partial V_D^2$ contributes only in this region, since both in the linear and in the saturation regions, the curves $I_D(V_D)$ are approximately lines. In this work, the V_D values corresponding to the maxima of each derivative were associated to the device's V_{knee} values. The curves in Figure 2.4, as well as the ones in Figure 2.5a,b, resulted from the DC simulations of the schematic depicted in Figure 2.2; the device's model was provided by the foundry.

A trade-off between CG and LO-power consumption is discussed in the
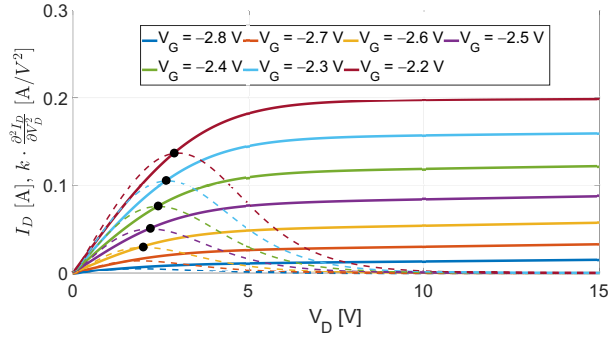
(a)
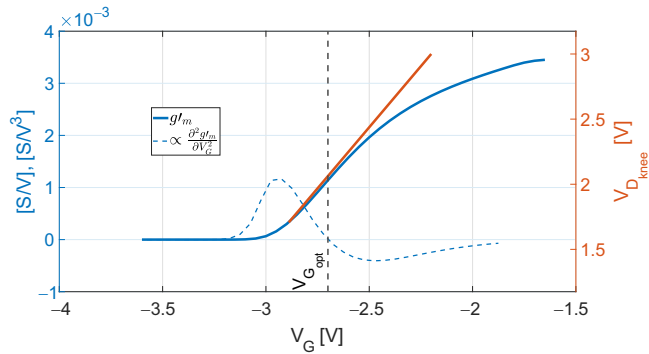
(b)

Figure 2.5: **(a)** Simulated I_D and a term proportional to its second derivative $k \cdot \frac{\partial^2 I_D}{\partial V_D^2}$ as functions of V_D for different values of V_G. **(b)** Simulated g'_m and a term proportional to its second derivative $\alpha \cdot \frac{\partial^2 g'_m}{\partial V_G^2}$ as functions of V_G for a fixed $V_D = +3\,\mathrm{V}$; on the right-axis, the knee-voltage $V_{D_{knee}}$ is reported. The $V_{G_{opt}}$ resulted in $\approx -2.65\,\mathrm{V}$.

following. For a better understanding of the concept, we consider a fixed value of V_D belonging to the region of the device's knee voltage, and we plot the $g'_m(V_G)$ for such a value, together with the $V_{knee}(V_G)$, as shown in Figure 2.5b. The value $V_{G_{opt}}$ representing a good compromise for our purposes corresponds to the inflection point of the $g'_m(V_G)$ function:

$$\left.\frac{\partial^2 g'_m}{\partial V_G^2}\right|_{V_G=V_{G_{opt}}} = \left.\frac{\partial^2}{\partial V_G^2}\left(\frac{\partial g_m}{\partial V_D}\right)\right|_{V_G=V_{G_{opt}}} = 0. \tag{2.2}$$

Infact, by naming the required LO-voltage as $V_{LO_{req}}$, for every V_G in the range $[\approx -2.9\,V, V_{G_{opt}}]$, the same ΔV_G would increase both the CG and the $V_{LO_{req}}$ by the same ΔCG and $\Delta V_{LO_{req}}$, while for $V_G > V_{G_{opt}}$, the same $\Delta V'_G = \Delta V_G$ leads to $\Delta CG' < \Delta CG$ and $\Delta V'_{LO_{req}} = \Delta V_{LO_{req}}$. Therefore, by biasing the device with such a value, from one side, the CG is achieved because $V_G > V_{TH}$, and from the other side, the injected LO power is employed in the most efficient way. For the device under consideration, it results in $V_{G_{opt}} \approx -2.65\,V$. It is worth noting that the result of the present analysis is independent on the chosen V_D, since the shape of the $g'_m(V_G)$ curves is approximately the same in the considered V_D range.

Drain-Side

As already observed in subsection 2.2.1, the CG is directly proportional to its first Fourier coefficient G_{m_1}. In [26], a closed form of the Fourier coefficient was derived, but it is only valid for passive DP mixers. In fact, it was derived under the condition of zero drain-bias, resulting in a time-varying waveform $g_m(t)$, approximately a cosine function with 50% of the duty cycle. Since the mixer of the present work is in the active configuration, a drain-bias greater than zero leads to a waveform significantly different with respect to the one resulting from a zero bias, as shown in Figure 2.1b.

In this work, we propose a method to maximize the first Fourier coefficient also for active DP mixers, as explained in the following. The results of the previous analysis led us to consider the $g_m(V_D)$ curve extracted for $V_G = -2.65\,V$. Therefore, the device's $g_m(V_D)$ was experimentally extracted in conditions of gate-bias $= -2.65\,V$. It is worth noting that the same $g_m(V_D)$ curve is useful for the extraction of $g_m(t)$ for different drain-bias and LO power values. For the case of passive DP mixers, the same method can be applied by fixing the drain-bias at zero and considering only the variation of the LO dynamic.
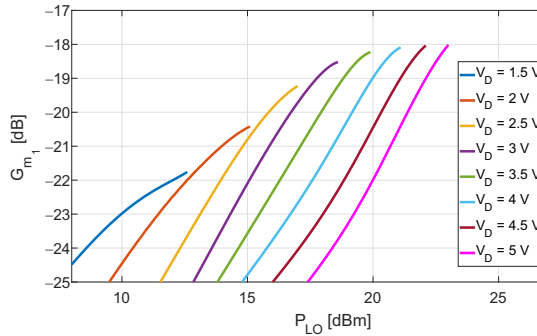
Figure 2.6: Experimentally extracted first Fourier coefficient G_{m_1} of the waveform $g_m(t)$ as a function of P_{LO} and V_D for $V_G = -2.65\,\text{V}$. The predicted minimum LO power necessary to maximize the coefficient is $\approx +20\,\text{dBm}$, achievable when the device's drain-bias is set at $\approx +3.5\,\text{V}$.

Figure 2.6 shows the results of the proposed method, in which the V_D was varied between $+1.5\,\text{V}$ and $+5\,\text{V}$ and the P_{LO} between $+5\,\text{dBm}$ and $+23\,\text{dBm}$. For each considered V_D, the P_{LO} was varied such as to keep the V_{LO} in the positive region of V_D. This choice is due to the fact that $g_m(V_D) = 0$ for $V_D < 0$, and thus, this region is not expected to contribute to the CG. In addition, the region of $g_m(V_D)$ around $V_D = 0$ is characterized by an abrupt change, and as such, the derivatives are expected to present oscillations, thus potentially increasing the intermodulations. The obtained results show the existence of a minimum LO power leading to the maximum G_{m_1} when the drain-bias is set to $\approx +3.5\,\text{V}$. This bias point was adopted in this work since the main objective was to test the potential of the DP mixers using GaN technology. The maximum G_{m_1} in the above conditions is obtained for $P_{LO} \approx +20\,\text{dBm}$.

Since the results presented in this subsection are based on an experimental-extraction procedure, a comment concerning the dispersion phenomena that affect GaN-based devices is necessary. The adopted g_m extraction procedure was carried out dynamically both at the gate and at the drain-side, with the aim of partially reducing both the self-heating and the trap effects, which represent the main causes of dispersion phenomena. In fact, the dynamic of the RF signal injected at the gate-side was such as to substantially exceed the threshold voltage, and the drain voltage was set to zero in the tran-

sition between the values of $V_D \neq 0$, reproducing a "pulsed-like" scenario. In the light of the recent efforts in the characterization of these dispersion phenomena [61–66], the adoption of a purely pulse-based characterization technique would provide a more accurate isolation of the dispersion effects; consequently, the method introduced in this work could lead to the identification of a more accurate result. However, the adopted extraction procedure is considered suitable for the purposes of this work.

2.3   DP Mixer Design

Given the high LO power levels involved in the investigation of GaN DP mixers, as confirmed both by the previous work in [33] and by the analysis of Section   2.2, the GaN-HEMT CGH40006S was considered suitable for this work.

Figure 2.7 shows the topology of the mixer prototype. The DP developed in this work follows the general circuit topology depicted in Figure 2.2. It resembles somehow the development of the supply-modulated power amplifier [57], where the main difference consists in the device drain-bias, which was set to a value much larger than its knee voltage, and as expected, the envelope signal only weakly modulated the device transconductance. In the present work, the device drain-bias was set lower than the one in [57] and brought closer to its knee voltage, in such a way that the LO signal strongly modulates the device transconductance [49]. The RF and LO matching networks were designed to operate in the S-band. A quarter-wavelength transmission line was used as both gate-biasing circuit and IF short-circuit. Capacitors and open stubs were used, where the latter reproduced the inductors operation but with less losses. The two capacitors closest to the gate- and drain-side, respectively, play the role of both DC and IF-blocking, as well as contributing to the RF and LO matching. For the extraction of the output signal (port 3) at the intermediate-frequency (IF), a quarter-wavelength transmission line was designed. At the same port, the drain-bias was injected by means of an external bias-Tee.

2.4   DP Mixer Characterization

Figure 2.8a shows the picture of the fabricated circuit, which was implemented in a 20 mil RO4350 laminate. The measurement procedure of the
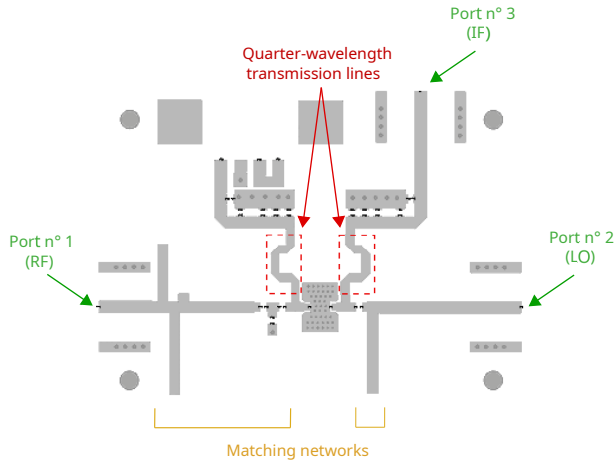
Figure 2.7: DP mixer layout in microstrip technology. The design was made for the operation in the S-band.

mixer was performed as follows. A single-tone characterization was carried out, during which the CG was measured as a function of the LO power and frequency for different values of gate-bias, followed by a two-tone characterization from which the IIP3 value was extrapolated. The experimental setup is represented in Figure 2.8b. The LO signal was generated by a synthesized source with the external amplifier required to get enough LO power, while the RF signal was generated by an arbitrary signal generator. The output power was measured by a spectrum analyzer. Finally, the mixer was involved in a radar setup to demonstrate its operation in an actual context.

2.4.1 Single-Tone Characterization

The DP mixer prototype described in Section 2.3 was first characterized with a drain-bias close to zero with the purpose of proving the limitations of the existing gate-bias method, as stated in Section 2.2. The passive DP mixer was chosen for this test since, being V_D close to zero, the device's transconductance only weakly depends on V_G, thus keeping the reflection coefficient at the gate-side approximately constant in the considered V_G range. This allows us to perform a consistent comparison between the $CG(P_{LO})$ curves obtained for different V_G values as reported in Figure 2.9. As it emerges from the results, the optimum gate-bias value according with the existing
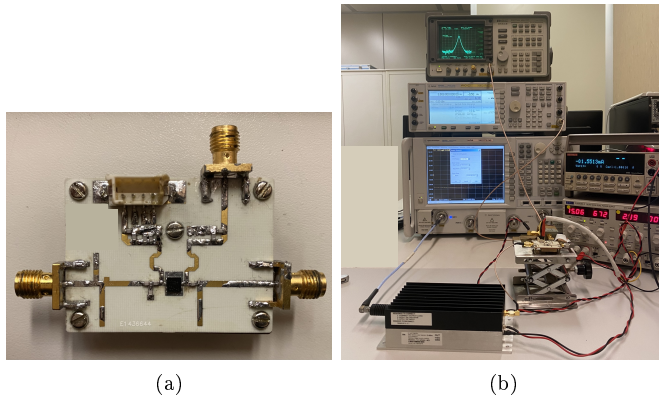
Figure 2.8: **(a)** Picture of the fabricated mixer prototype and **(b)** experimental setup for CG and IIP3 measurements.

method allows to achieve the maximum CG, but at the cost of a large P_{LO} of $\approx +29\,$dBm for the device employed in this work. In particular, it can be noticed that increasing P_{LO} from $+21\,$dBm to $+29\,$dBm, the CG increases just over $1\,$dB.

The results of the single-tone characterization for the active DP mixer in the bias conditions proposed in this work are shown in Figure 2.10a. The DP mixer reached $CG = +10\,$dB for the P_{LO} value predicted by the analysis, about $+20$ dBm, with RF and LO signals at 3.7 and 3.74 GHz, respectively. The same figure also reports the Harmonic-Balance (HB) simulation results, which involve the layout characterization made by an electromagnetic simulator.

2.4.2   Two-Tone Characterization

Under the above conditions of bias and P_{LO}, a two-tone signal of frequencies $3.709 \pm 0.002\,$GHz was injected at the port 1, and its power was swept from -25 to $+8\,$dBm. Figure 2.10b reports the output power at the IF frequency of $43\,$MHz and the third-order intermodulation product (IMP3) power at $45\,$MHz as functions of the input power. From the curves, an IIP3 value of about $+11\,$dBm was extrapolated. The same figure also reports the HB simulation results.

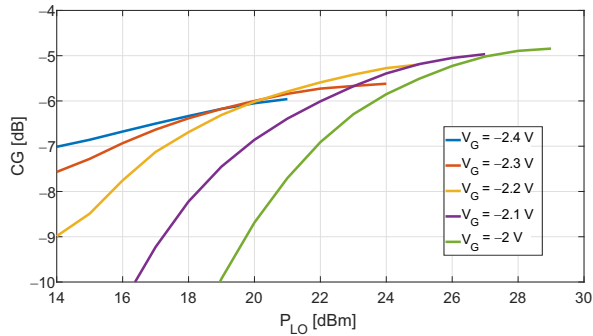Both the CG and the IIP3 results exceed the values reported so far in

Figure 2.9: DP mixer's measured CG as a function of P_{LO} with the gate-bias as parameter and drain-bias $+0.2\,\text{V}$.

the literature for single-ended DP mixers.

2.4.3   FMCW Radar-Mode Setup

An FMCW radar-mode setup test bench was implemented with the aim to demonstrate the DP mixer operation in an emulated radar context. Figure 2.11a shows the conceptual schematic, and the picture in Figure 2.11b shows the adopted experimental setup. A frequency-modulated signal around 3.7 GHz, represented in Figure 2.11c, was generated by the sweep oscillator and injected in a splitter. One of the two output ports of the splitter was connected to the external amplifier, thus emulating the LO signal, and the other one was connected to the delay line, thus emulating the return RF signal.

The adopted setup allowed us to obtain an output IF signal of a few kHz as explained in the following. The delay line introduced a time delay of 85 ns, and since the swept oscillator constraints concerning the minimum raise and fall times of the generated ramp were 10 ms and 4 ms, respectively, a frequency-modulated signal of 1 GHz bandwidth was used. In this way, the IF signals of frequencies about 8.5 kHz and 21.25 kHz were predicted.

Figure 2.11d shows the resulting output spectrum, confirming the predictions discussed above. It is worth noticing that the signal at 21.25 kHz results in more dispersion since it is related to the falling side of the ramp, which is not perfectly controlled by the instrument.

(a)

(b)
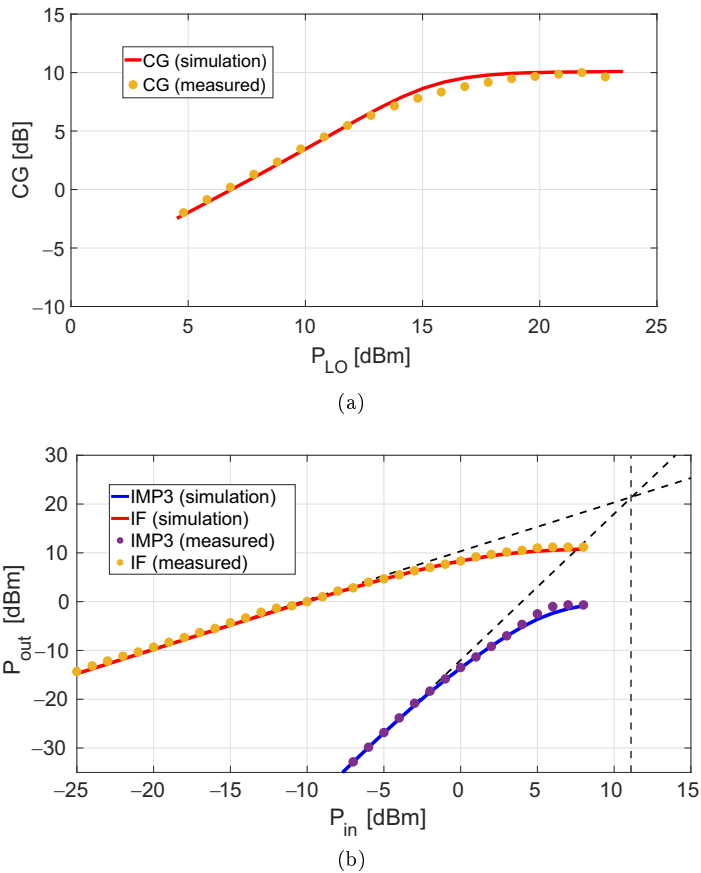
Figure 2.10: DP mixer's single-tone and two-tone characterization in the gate- and drain-bias conditions of $-2.65\,\mathrm{V}$ and $+3.5\,\mathrm{V}$, respectively. (**a**): Simulated and measured CG as a function of P_{LO}. (**b**): Simulated and measured output power of IF and IMP3 tones as a function of the input power for $P_{LO} = +20\,\mathrm{dBm}$.

(a)

(b)

(c)

(d)
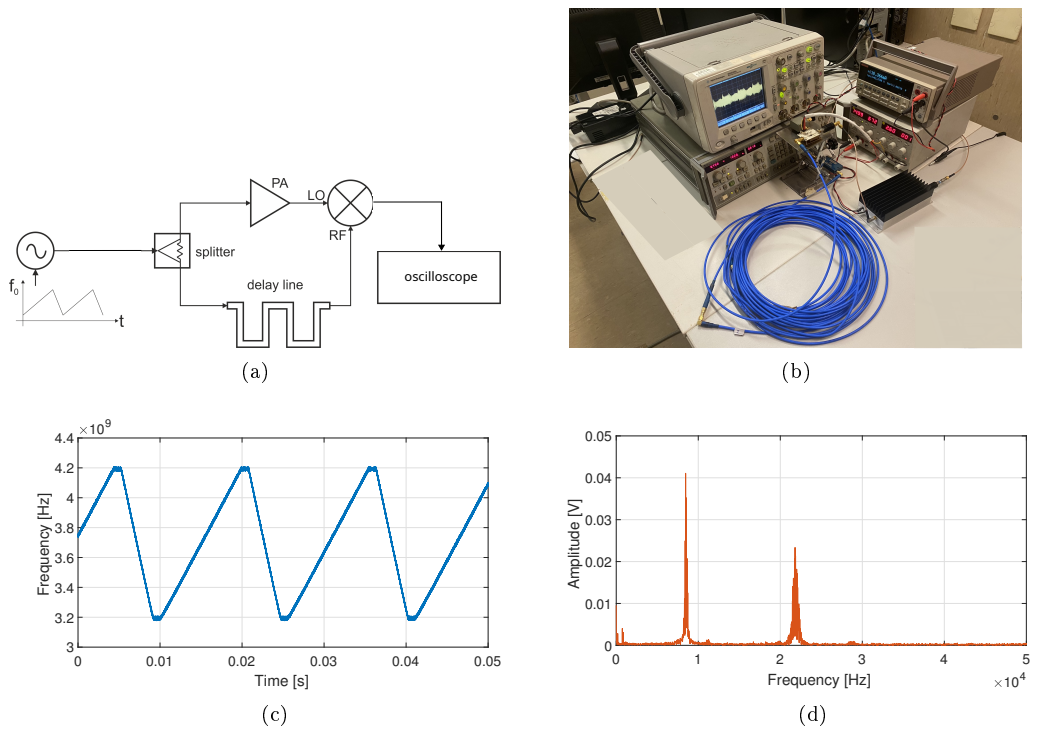
Figure 2.11: (**a**) Conceptual schematic of the radar setup mode; (**b**) experimental radar setup mode; (**c**) generated FMCW signal; (**d**) output spectrum of the DP mixer.

2.5   DP and Resistive Mixer Comparison

With the purpose of providing a term of comparison in the radar context, a resistive mixer was designed and fabricated using the same technology. The DP and the resistive mixers share the same circuit topology, only differing in the fact that the first operates with the RF signal injected at the port 1 and the LO signal at the port 2, and the latter operates with these two signals exchanged with each other [22, 25]. This allowed us to easily perform a consistent comparison since the same circuit layout of Figure 2.7 can be adopted for the design of the resistive mixer. Since the drain-bias is zero for a resistive mixer, a proper capacitor of the drain-side's matching network was selected in order to optimize the RF matching.

2.5.1   Resistive Mixer Characterization

The CG of the resistive mixer was measured as a function of the LO power and for different bias values to search for a good compromise between CG and P_{LO} consumption. The results are reported in Figure 2.12a, and the selected combination is +16 dBm and −3 V for the P_{LO} and V_G, respectively. Under these conditions, a two-tone signal at the same frequencies as for the DP-configuration was applied at the port 2. The input power was swept from −15 to +10 dBm, and Figure 2.12b shows the output IF and IMP3 power tones as functions of the input power. The measured value of IIP3 was about +19.5 dBm. As for the DP-mixer, the measurement results were supported by the HB simulations. The simulation results are not shown in Figure 2.12a for clarity.

2.5.2   Comparison for Radar-Mode Operation

The resistive mixer was involved in the same radar setup as in Figure 2.11b and the same ramp as in Figure 2.11c was employed. The output spectrum of the resistive mixer is reported in Figure 2.13 overlapped with the one of the DP mixer. The measurements were carried out while the two mixers operated with the same RF and LO power levels, corresponding to about −18 and +10 dBm, respectively. The above conditions allowed us to carry out a clean comparison between the two mixers, but they clearly penalized the DP mixer. Nevertheless, it showed an SNR of +39.7 dB versus the +34.7 dB of the resistive mixer, demonstrating that it is a valid alternative even in
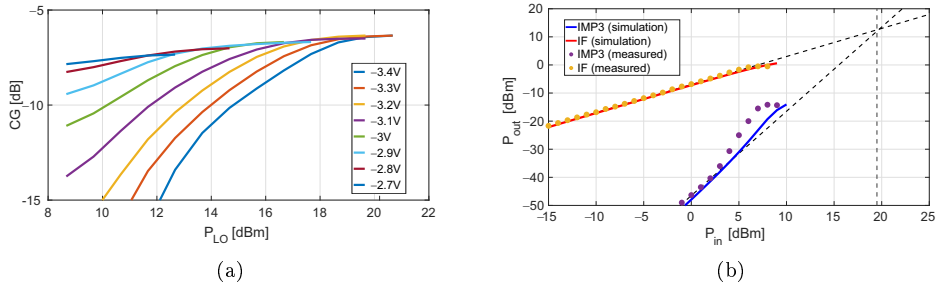
Figure 2.12: (**a**) Measured CG as a function of the LO power with the gate-bias as parameter for the resistive configuration; (**b**) simulated and measured output power IF and IMP3 tones as a function of the input power for the resistive configuration, at gate-bias of -3 V, and LO $= +16$ dBm.

conditions of lower LO power than its optimal value.

Differently from Section 2.4, in which the limitations of the mixer's performance had to be tested and thus its was driven with high LO power levels, in the present section, the proper operation of the mixer was also demonstrated in more relaxed conditions of LO. The results could be significant in view of its implementation for applications with stringent power requirements.

2.6   Conclusions

In this work, the first DP mixer in GaN is presented, showing $+10$ dB of CG and $+11$ dBm of IIP3. The high drain-to-source breakdown voltage of this technology is at the basis of both high gain and high linearity. In Table 2.1, the state-of-the-art performance of single-ended DP mixers in terms of gain and linearity is reported, among which this work shows by far the best performance. A figure-of-merit aimed to quantify the efficiency with which the P_{LO} is employed is reported in the same table. The mixer was also demonstrated in actual radar setup mode. In both the multi-tone and radar modes, the DP mixer was compared with the resistive mixer. In the latter mode, the DP exhibited a better SNR, respectively, 39.7 dB versus 35.7 dB. This component results in a good candidate for radar systems with
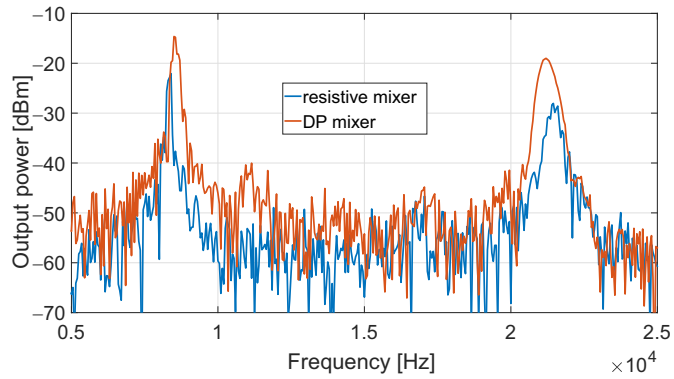
Figure 2.13: Output spectrum of the DP and resistive mixers while operating in radar setup.

many channels where complexity and performance are of concern.

Table 2.1: State-of-the-art of single-ended drain-pumped mixers.

Work	Tech.	Band	CG [dB]	IIP3 [dBm]	V_D [V]	P_d [mW]	P_{LO} [dBm]	P_{LO}-CG [dBm]
[49]	GaAs MES-FET	X	+1.5	-	+0.7	17*	+10.5	+9
[27]	GaAs pHEMT	Ku	+2.5	0	+1.1	-	+15	+12.5
[26]	SOI CMOS	Ka	−4.6	+4 *	0	0	+7.5	+11.6
[25]	GaAs mHEMT	G	−7*	-	+0.2	0.55	+5	+12
[22]	InP HEMT	F	−6.5	-	0	0	+6	+12.5
t.w.	GaN HEMT	S	+10	+11	+3.5	87	+20	+10

* Estimated from plots.

Chapter 3

Linearity performance of GaN and GaAs active gate-pumped mixers

In this chapter, a detailed analysis of the third-order intermodulation products occurring in a GaN HEMT operating as an active gate-pumped mixer was presented. As expected, the high drain-to-source breakdown-voltage of the GaN technology makes the output conductance contribution negligible to the overall mixer operation. A comparison in terms of linearity between GaN and GaAs-based active gate-pumped mixers was then carried out. This was accomplished by elaborating the data extracted from the physical devices, thus allowing for an experimental-based comparison without manufacturing the circuits. [1]

3.1   Introduction

The results showed in chapter 2 laid the foundations for pursuing the investigation on the active mixers. While from the one side the high drain-to-source breakdown-voltage of the GaN technology allows a larger dynamic

---

[1]This chapter was part of the paper published as "A Highly Linear Ka-band GaN-on-Si Active Balanced Mixer for Radar Applications" in the *IEEE Transactions on Circuits and Systems I: Regular Papers* [44].

of the PLO, thus making the drain-pumped mixer achieve better performance, on the other side this GaN-feature is expected to also benefits the gate-pumped configuration. Indeed, in gate-pumped mixers the drain-bias is commonly in a region of flatness drain-source I/V characteristics, and being such region more extended in GaN devices with respect to the other technologies, it is expected that the relative drain-to-source conductance only weakly contribute to the overall nonlinear mechanism. This fact doesn't occur in the drain-pumped configuration, since the drain-bias is close to the device knee-voltage, leading to a strongly conductance modulation.

Among the active single-ended configurations, the gate-pumped is undoubtedly the most documented [29, 45–47, 67]. In a recent work, [67], the trade off between DC bias and LO power was investigated, and over the years the mixer was proposed for wireless communications [45, 46], high-temperature operations [47] and also radar [29]. In particular, in [29] the mixer implemented a GaN-based device, and the high-linearity feature was experimentally observed, but without providing any explanation about it.

In this work, we analyze the IMP3 occurring in a GaN-HEMT gate-pumped mixer as a function of the gate bias and for different values of the local oscillator power and output load termination. The results of the analytical analysis, considering only the device nonlinear transconducance, and the ones of the HB method, considering the complete HEMT foundry model, were compared to each other.

An analytical method was then adopted for the prediction of the IIP3 of a GaN and GaAs-based gate-pumped mixer, respectively. The calculations are based on the data extracted from the two physical stand-alone devices. The same extraction procedure, as well as the same data elaboration, were applied in the two cases and the results compared to each other.

3.2 Nonlinear analysis of GaN-based gate-pumped mixers

3.2.1 Identification of the dominant nonlinear contributions

It is well known in the literature as a whole that the dependency of the drain current upon the terminals voltages is the most important nonlinear contribution in general field-effect transistor applications [59], [32]. In order
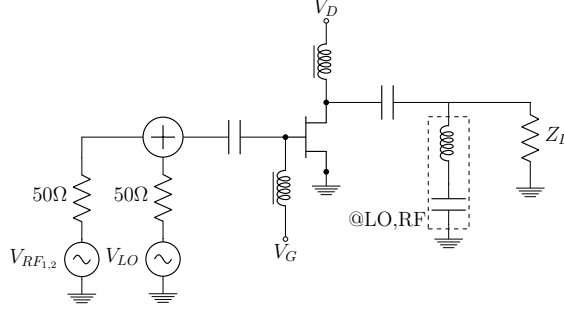
Figure 3.1: A conceptual schematic for the active mixer, used for the IMP3 analysis.

to enable the analysis of the IMPs in a mixer, we assume a time-varying small-signal drain current component of $i_d(v_g, v_d)$ derived by expansion in Taylor's series up to third order as follows, [54],

$$
\begin{aligned}
i_d(v_g, v_d) =& \frac{\partial I_d}{\partial V_g} v_g + \frac{\partial I_d}{\partial V_d} v_d + \frac{1}{2} \left[\frac{\partial^2 I_d}{\partial V_g^2} v_g^2 \right. \\
&+ \frac{\partial^2 I_d}{\partial V_d^2} v_d^2 + 2 \frac{\partial^2 I_d}{\partial V_g \partial V_d} v_g v_d \right] \\
&+ \frac{1}{6} \left[\frac{\partial^3 I_d}{\partial V_g^3} v_g^3 + 3 \frac{\partial^3 I_d}{\partial V_g^2 \partial V_d} v_g^2 v_d \right. \\
&\left. + 3 \frac{\partial^3 I_d}{\partial V_g \partial V_d^2} v_g v_d^2 + \frac{\partial^3 I_d}{\partial V_d^3} v_d^3 \right] \\
\equiv& g_m v_g + g_{ds} v_d \\
&+ g_{m2} v_g^2 + g_{d2} v_d^2 \\
&+ g_{m1d1} v_g v_d + g_{m3} v_g^3 \\
&+ g_{m2d1} v_g^2 v_d + g_{m1d2} v_g v_d^2 + g_{d3} v_d^3,
\end{aligned}
\tag{3.1}
$$

where the time dependence of all coefficients due to the LO pump has been dropped, to simplify the notation. The approach we adopted in this work relies on the time-varying Volterra series analysis, [31].

Unlike resistive mixers, for which cross terms are also important [68], in active mixers the device drain terminal is normally short-circuited at the RF and LO signals, thus making the nonlinear transconductance the main contribution to the drain current. This fact, together with the high drain-to-

source voltage breakdown of GaN devices, led us to neglect the contributions coming from the drain-to-source conductance. Limiting our considerations to the third-order components

$$
\begin{aligned}
v_g(t) &= v_{g1}(t) + v_{g2}(t) + v_{g3}(t) \\
v_g^2(t) &= v_{g1}^2(t) + 2v_{g1}(t)v_{g2}(t) \\
v_g^3(t) &= v_{g1}^3(t),
\end{aligned}
\tag{3.2}
$$

taking v_{gn} to be the voltage of the n-th order mixing products, the well-known device nonlinear third-order drain current is

$$
i_{d3}(t) \approx g_{m3}(t)v_{g1}^3(t) + 2g_{m2}(t)v_{g1}(t)v_{g2}(t).
\tag{3.3}
$$

We are now going to employ a qualitative approach to physically understand, in down-conversion operation mode, the IMP3 component of our interest, that is, the one at $\omega_{IF_{IMP3}} = 2\omega_{RF_1} - \omega_{RF_2} - \omega_{LO}$; with $\omega_{RF_{1,2}}$ being the angular frequencies of the two RF signal tones applied to the mixer and ω_{LO} the corresponding angular frequency of the local oscillator. For this purpose, we rewrite (5.2) in the frequency domain and, using the matrix form of the convolution product, [31], [69], [55], we obtain

$$
\mathbf{I_{d3}} \approx \mathbf{G_{m3}} \mathbf{V_{g1}^{(3)}} + 2\mathbf{G_{m2}} \mathbf{V_{g1;2}^{(3)}},
\tag{3.4}
$$

where $\mathbf{G_{m3}}$, $\mathbf{G_{m2}}$ are conversion matrices and $\mathbf{I_{d3}}$, $\mathbf{V_{g1}^{(3)}}$ and $\mathbf{V_{g1;2}^{(3)}}$ are matrices in which each row contains phasors with a specific LO order contribution and each column contains phasors at a specific third-order RF mixing product.

The stronger signals present at the gate terminal are those due to the excitation, $\omega_{RF_{1,2}}$, and under the assumption of short-circuit terminating the drain terminal at RF and LO signals, those at $\omega_{IF_{1,2}} = \omega_{RF_{1,2}} - \omega_{LO}$, due to

the feedback. This allows assuming that the $\mathbf{I_{d3}}$ component at $\omega_{IF_{IMP3}}$ is

$$
\begin{aligned}
I_{d3}(\omega_{IF_{IMP3}}) \approx & G_{m3_1} V_{g1}^{(3)}(2\omega_{IF_1} - \omega_{RF_2}) \\
& + G_{m3_0} V_{g1}^{(3)}(\omega_{RF_1} + \omega_{IF_1} - \omega_{RF_2}) \\
& + G_{m3_0} V_{g1}^{(3)}(2\omega_{IF_1} - \omega_{IF_2}) \\
& + G_{m3_{-1}} V_{g1}^{(3)}(2\omega_{RF_1} - \omega_{RF_2}) \\
& + G_{m3_{-1}} V_{g1}^{(3)}(\omega_{RF_1} + \omega_{IF_1} - \omega_{IF_2}) \\
& + G_{m3_{-2}} V_{g1}^{(3)}(2\omega_{RF_1} - \omega_{IF_2}) \\
& + 2G_{m2_1} V_{g12}^{(3)}(2\omega_{IF_1} - \omega_{RF_2}) \\
& + 2G_{m2_0} V_{g12}^{(3)}(2\omega_{IF_1} - \omega_{IF_2}) \\
& + 2G_{m2_{-1}} V_{g12}^{(3)}(\omega_{IF_1} - \omega_{IF_2} + \omega_{RF_2})
\end{aligned}
\tag{3.5}
$$

where $G_{m\alpha_k}$ is the component of the $\mathbf{G_{m\alpha}}$ conversion matrix corresponding to the k-th Fourier coefficient of the $g_{m\alpha}(t)$ waveform.

In radar applications, the IF spectrum is normally limited to a few MHz, leading to the extrinsic drain-to-source resistance R_s being the only feedback element. In addition, since in the GaN-HEMT state-of-the art processes this value is normally lower than 1 Ω, the IF components from the mixer output to the input can be neglected. Such observations lead to a further approximation for (3.5):

$$
I_{d3}(\omega_{IF_{IMP3}}) \approx G_{m3_{-1}} V_{g1}^{(3)}(2\omega_{RF_1} - \omega_{RF_2})
\tag{3.6}
$$

which reveals that the term $G_{m3_{-1}}$ is the most important for the IMP3 process of the active gate-pumped mixer.

In order to implement (3.6), the $I_D(V_G)$ curve was evaluated at the drain section, and the determination of its first three derivatives for each V_G was obtained by polynomial fitting. Afterwards, a single-tone Harmonic-Balance simulation provided the time-domain waveforms at the extrinsic gate and drain terminals that, together with the knowledge of the derivatives of $I_D(V_G)$, led to the curves $g_m(t)$, $g_{m2}(t)$ and $g_{m3}(t)$. Studying their Fourier transform coefficients, the identification of the corresponding conversion matrices $\mathbf{G_m}$, $\mathbf{G_{m2}}$ and $\mathbf{G_{m3}}$ is then possible, and so is the subsequent application of the nonlinear currents method, [59], once provided the term $I_{d3}(\omega_{IF_{IMP3}})$. The procedure starting from the evaluation of the waveforms at the gate and drain was repeated for different V_G bias values and for different PLO levels.

3.2.2   Analysis results

The response of the IMP3 as determined by (3.6) was compared with the Harmonic-Balance simulations of the circuit in Fig. 3.1 by considering a 8 x 50 μm GaN HEMT, whose model was provided by the foundry. The results are shown in Fig. 3.2. In the analysis the LO frequency was set at 1 GHz, the two tone RF signal set at -10 dBm with 1 MHz separation between tones, and the IF frequency at 10 MHz. The comparison is provided across V_G for two different PLO levels, respectively 15 dBm and -8 dBm, and for two different load terminations, respectively 5 and 20 Ohm. In the same figure the converted components are also shown, as provided from the term g_m in (A.1), whose separation from the corresponding IMP3 is more descriptive of the linearity of the mixer.

From the comparison, as the first consideration, we can see the similarity between the response of the (3.6) with the Harmonic Balance simulation. The LO frequency of 1 GHz used in the Harmonic-Balance simulations resulted to be the maximum one leading to an accuracy less than 1 dB, thus demonstrating the accuracy of the assumptions that have led from (A.1) to (3.6). This confirms that the GaN-HEMT operates as an active mixer with great accuracy as a simple nonlinear transconductance under the above discussed assumptions.

3.3   Experimental-based IIP3 prediction of GaN and GaAs gate-pumped mixers

With the aim of performing a consistent comparison in terms of linearity between gate-pumped mixers, implemented in GaN and GaAs technologies respectively, we have considered two sample HEMT devices whose characteristics are reported in Table 3.1. The figure of merit adopted for the comparison is the IIP3.

For this purpose, we adopted the analysis discussed in Section 3.2.1. In order to identify the term, $G_{m3_{-1}}$, in (3.6), concerning the major contribution of IMP3, we adopted an experimental procedure aimed at removing the low-frequency dispersion effects that makes unsuitable the differentiation of measured DC data. Indeed, the procedure implemented in the Section 3.2 for the extraction of $g_m(V_G)$, was replaced by the more suitable one described in [59]. For this purpose, we applied a single tone at 50 MHz with

(a)

(b)
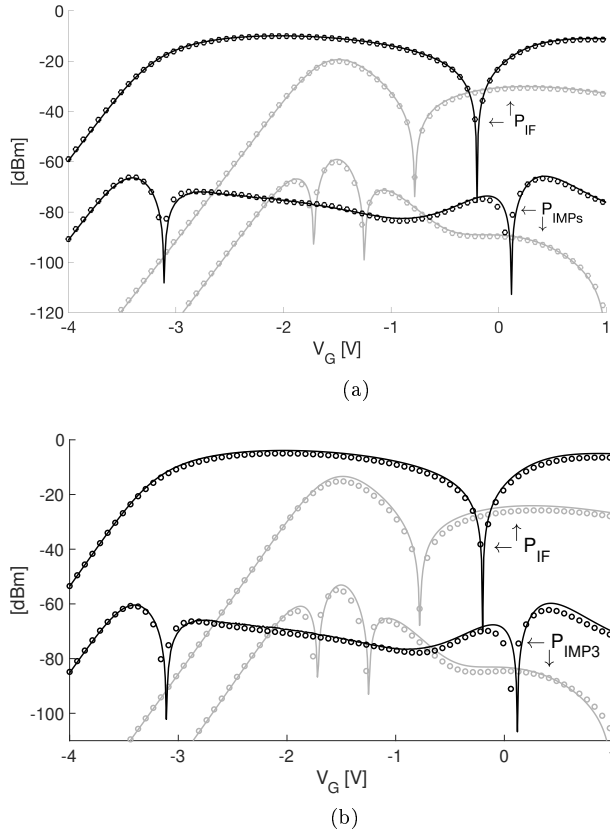
Figure 3.2: Evolution of PIF and IMPs across bias for $P_{LO} = -8$ dBm
(gray) and $P_{LO} = 15$ dBm (dark). The lines are time varying Volterra series
analysis results, while the symbols are the harmonic balance results; RF
level -10 dBm, IF frequency 10 MHz and two tones separation 1 MHz, LO
frequency 1 GHz. For the device under consideration, i.e., the GaN-on-Si
D01GH OMMIC process, $V_G = -1.5$ V corresponds to the pinch-off. In (a)
the IF load was set to 5 Ohm, while in (b) it was set to 20 Ohm.

Table 3.1: Characteristics of the GaN and GaAs HEMTs samples adopted
for the linearity comparison

	GaAs	GaN
process	WIN PP10-20	OMMIC D01GH
gate length	100 nm	100 nm
gate periphery	8x25 μm	4x30 μm
power density	1 W/mm[1]	4 W/mm
bias	Vds=4 V, Id=0 mA	Vds=10V, Id=0 mA
max current	Idss=450 mA/mm at 12V	Idss=1200 mA/mm at 4V
f_t	120 GHz	110 GHz

at 29 GHz[1].

available power level $P_{av_{dBm}} = -7\,\text{dBm}$ at the gate terminal of the devices
under test, with the gate bias voltage spanning between -3 V and +0.5 V,
while the corresponding drain output power levels, P_{rf} were measured. This
procedure permits to extract experimentally the dependence of the extracted
g_m on V_G, by using the relation

$$g_m = \sqrt{\frac{P_{rf}}{4P_{av}}\frac{1}{R_0^2}},\tag{3.7}$$

where P_{av} and P_{rf} are linear quantities, and $R_0 = 50\Omega$ is the input and out-
put terminations. In this operation condition, we can assume negligible the
parasitic gate capacitance. Since the $g_m(V_G)$ shape recalls the Gaussian-like
function shape, the former has been fitted with sum of Gaussian functions,
and the transconductance higher order derivatives were determined analyti-
cally. A similar approach is used in [54] for the nonlinear analysis of active
mixers.

Then, for both the devices, we calculated the time-domain gate waveform
$g_m(t)$ and $g_{m3}(t)$ having considered a sinusoidal $V_G(t)$ voltage, about a gate
bias corresponding at the pinch-off voltage, that is -1.75 V and -1 V for the
GaN and GaAs HEMTs respectively. The knowledge of the time-domain gate
waveform leads to the $g_m(t)$ and $g_{m3}(t)$ curves, from which the extraction of
their Fourier coefficients $G_{m_{-1}}$ and $G_{m3_{-1}}$ is straightforward. As discussed
in the Section 3.2, the extraction of the Fourier coefficients was repeated for

different values of the magnitude of $V_G(t)$ as to reproduce the input available PLO variation. Finally the IIP3 was evaluated by the

$$V_{RF_{IIP3}} = \sqrt{\frac{4}{3} \frac{|G_{m_{-1}}|}{|G_{m3_{-1}}|}}, \tag{3.8}$$

which relates the IF and the IMP3 components by respectively the terms $G_{m_{-1}}$ and $G_{m3_{-1}}$.

Fig. 3.3 shows the comparison between the IIP3 obtained by applying the same procedure described above to the two sample devices. These data assume that both the LO and RF signals are matched to the HEMTs gate terminal, while the analysis, implicitly, assumes that the devices were terminated with short circuit at both the RF and the LO frequencies, at the drain terminal; finally, it is worth to recall that the IIP3 does not depend upon the termination, as it is a ratio between power levels.

From the above comparison, we can observe that both the devices exhibit a maximum in the IIP3 versus PLO behavior, while the GaN device reaches the highest level of 16.7 dBm, the GaAs one reaches the level of 13.3 dBm; additionally, the GaN device can provide higher linearity when driven by a larger LO level. This result fully justifies the motivation of the work as it represents, at device level, the inherent capability of the GaN devices with respect to GaAs devices based on a consolidated characterization technique. As a final remark we have to consider that the estimated IIP3 from Fig. 3.3, does not consider the effect of input combiner losses at high frequency and the RF power splitting among two or more devices. These are normally present in experimental mixer prototypes and lead to a significantly increase the overall IIP3 behavior.

3.4   Conclusions

The IMP3 analysis revealed that, as expected, the device transconductance is by far the main contribution in the nonlinear mechanism of GaN gate-pumped mixer. A subsequent analysis based on experimental data allowed to perform a comparison between GaN and GaAs-based active gate-pumped mixers in terms of linearity. The same procedure of data-extraction and analytical calculations on both the devices revealed that the GaN is capable of reaching IIP3 values higher than the GaAs counterparts. This work provides the theoretical foundation for the development of a GaN HEMT active
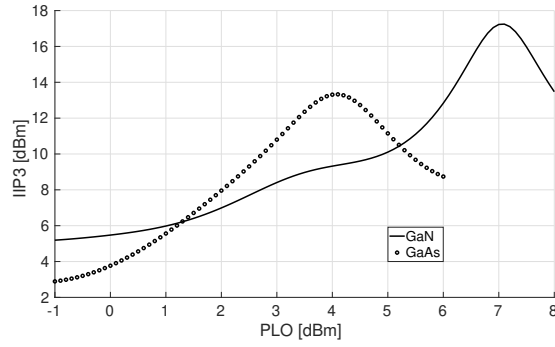
Figure 3.3: Experimental IIP3 versus PLO comparison between GaAs and GaN HEMTs.

gate-pumped mixer.

Chapter 4

A highly-linear active GaN mixer for radar applications

In this chapter, a highly linear active mixer in Gallium Nitride on Silicon (GaN-on-Si) monolithic microwave integrated circuit (MMIC) technology, operating in Ka-band for radar applications is introduced. It exhibits a LO balanced topology of gate-pumped mixers based on HEMT and operates in down-conversion mode. Its design principles and the theoretical foundation of its linearity features resulting from both the high power handling capability of GaN-on-Si HEMTs and the corresponding high applied LO level are presented. An extensive characterization based on excitation of a prototype by broadband continuous wave signals and frequency modulated continuous wave signals validates both the analytical treatment of its linearity and the design of the prototype of the mixer. In the 35–40 GHz operating band, this prototype exhibits a state-of-the-art input referred third order intercept point that reaches 39.1 dBm, and a maximum input referred second order intercept point of 39.4 dBm, with a a corresponding conversion gain of -5.2 dB, and LO level of 24 dBm. [1]

---

[1] This chapter was part of the paper published as "A Highly Linear Ka-band GaN-on-Si Active Balanced Mixer for Radar Applications" in the *IEEE Transactions on Circuits and Systems I: Regular Papers* [44].

4.1   Introduction

The results in terms of SNR obtained by the comparison conveniently carried-
out between drain-pumped and resistive GaN mixers, as shown in chapter 2,
led us to consider the active configuration for the development of a mixer for
radar applications. The active gate-pumped configuration was then consid-
ered, as to exploit the GaN high drain-to-source breakdown-voltage in such
a way as to make the mixer generate reduced intermodulation products, as
discussed in the Section 3.2 of the chapter 3. Then, the higher linearity
reached by the GaN-based gate-pumped mixer with respect to the GaAs-
based one, as predicted by the experimental-based analysis of section 3.3 of
chapter 3, finally laid the foundations for the development of a highly-linear
GaN active mixer for radar applications.

   The mixer was designed to operate in the Ka-band. A balanced structure
was adopted, as to both improve the isolation and to cancel out the second-
order intermodulation products, while a high-dynamic PLO was employed
for the additional reduction of the IMP3. The phenomenon concerning the
IMP3-reduction when the PLO increases has been shown in the literature
for different classes of mixers, but only a heuristic explanation has been
given, [18], [19]. In [20] was introduced a closed formulation describing the
relation of the input referred IIP3 with the PLO, but without providing
any analytical treatment. In [18], the drop in the levels of the IMPs with
increased PLO is related to the shorter transition between the device's ON
and OFF states as the PLO increases. In this work, for the first time is
provided, by using the time-varying power-series approach, an analytical
explanation for the decrease of IMP3 when the PLO increases.

4.2   Theoretical foundations on the impact of LO on linearity

The dependency of the IMP3 in an active mixer can be conveniently observed
by running Harmonic-Balance simulations of the mixer schematically shown
in Fig. 3.1 by considering ideal passive components and the $8 \times 50 \mu$m 0.1 um
GaN-on-Si HEMT device model available in the OMMIC foundry process
design kit. In particular, we focused our attention on the IMP3 levels result-
ing from the application of local oscillator signals at different power levels,
PLO, and frequencies. In addition, we considered the response for different

IF load terminations: for each of the cases we applied two RF tones spaced at 1 MHz, with total power level of -10 dBm, and center IF frequency set to 10 MHz. The four considered cases result from the combination of two different IF load terminations, namely 20 Ω and 50 Ω IF load terminations, and two LO frequencies, namely 1 GHz and 38 GHz. A comparison of the IMP3 power level versus PLO is provided in Fig. 4.1. As expected, their trends highlight a generalized decrease of the IMP3 level, for all the considered cases, from which we can conclude that the main mechanism responsible for the decrease in the IMP with increasing PLO remains unchanged with different load terminations and LO frequencies.
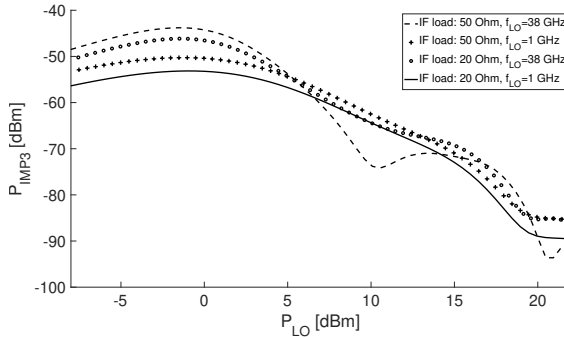

Figure 4.1: Harmonic balance simulations of IMP3 power level as a function of P_{LO} for gate-pumped GaN-HEMT mixer; the bias point is $V_{DS} = 10$ V, $V_{GS} = -1.6$ V.

Considering the results of the chapter 3, this result allowed us to consider only the device transconductance for the following analysis without harming in generality, thus significantly simplifying the discussion.

By inheriting the work of transconductance-extraction performed in the chapter 3, we consider the $g_{m3}(V_G)$ shown in Fig. 4.2a, and the corresponding time domain evolution of the $g_{m3}(t)$ as a function of the PLO, shown in Fig. 4.2b at three different gate bias voltages about the device pinch-off. From the latter picture, we can observe that $g_{m3}(t)$ exhibits significant symmetries, which play a key role in the corresponding generation of the minima and maxima of the IMP3. Considering firstly the case at LO level -8 dBm, which is the graph at the top of Fig. 4.2b, we can see that biasing the gate at the pinch-off maximizes the amplitude of $g_{m3}(t)$, and leads the waveform to

have a half-wave symmetry, that is, $g_{m3}(t + T/2) = -g_{m3}(t)$, with T being the period of the LO waveform. This causes its odd Fourier coefficients to be maximized, among which is $G_{m3_{-1}}$, whose dependence on the bias is represented in Fig. 4.2c. In contrast, by shifting the gate bias of ± 0.2 V about the pinch-off, the generated waveforms exhibit lower amplitudes and get closer to the opposite symmetry $g_{m3}(t+T/2) \approx g_{m3}(t)$, leading the coefficient $G_{m3_{-1}}$ to be minimized. This behavior is consistent with that already observed in Fig. 4.1, where we can see that the IMP3 does not show significant variation up to LO of a few dBm, beyond which a different mechanism occurs instead.

For PLO = 4 dBm the gate bias at the pinch-off leads the time-domain waveform at the extrinsic gate side to capture the whole variation of g_{m3} versus V_G in Fig. 4.2a, thus providing the $g_{m3}(t)$ waveforms shown in the middle graph of Fig. 4.2b with respect to different gate biases. A further increase in PLO makes the corresponding $g_{m3}(t)$ resemble single-cycle tone bursts, with progressively shorter duration of the burst, as shown in the graph at the bottom of Fig. 4.2b for a PLO level of 15 dBm.

Giving $g_{m3}(t)$ of Fig. 4.2b, the following approximation permits capturing the dependence on PLO > 4 dBm

$$
\begin{aligned}
g_{m3}(t,a) \approx & A \cdot 0.2 sin(2\pi\frac{2}{T}a(t - T/4)) \\
& - B \cdot 0.2 sin(2\pi\frac{2}{T}a(t - 3T/4)),
\end{aligned}
\tag{4.1}
$$

where $a \propto$ PLO is the ratio between the period and the duration of the signal and A and B $rect(\frac{a(t-T/4)}{T/2})$ and $rect(\frac{a(t-3T/4)}{T/2})$ respectively, we obtain

$$
\begin{aligned}
G_{m3_{-1}}(a) \triangleq & \frac{1}{T}\int_0^T g_{m3}(t,a)e^{j2\pi\frac{1}{T}t}\,dt \\
= & \frac{-4a \cdot \sin(\pi/2a)}{5\pi(-1 + 4a^2)}
\end{aligned}
\tag{4.2}
$$

from which we can observe that as the PLO level increases, the numerator of (4.2) tends to be independent of a, making it evident that $G_{m3_{-1}}$ decreases.

The Fig. 4.2c shows a comparison of the coefficient $G_{m3_{-1}}$ for the PLO level investigated and different biases. From the picture is evident that for a PLO level of 15 dBm, the behavior is significantly flat and has the lowest average among those analyzed.

We can briefly discuss that following an analogous derivation, we can easily derive the term $G_{m_{-1}}$, which governs the IF component; its behavior
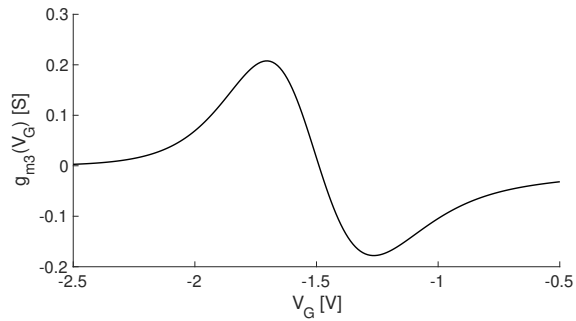
(a) g_{m3} versus V_G
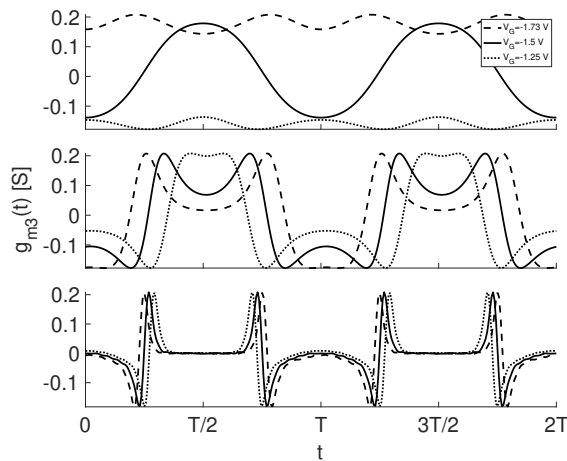
(b) $g_{m3}(t)$for three different V_G with PLO=-8 dBm (top), PLO= 4 dBm (middle) and PLO=15 dBm (bottom)
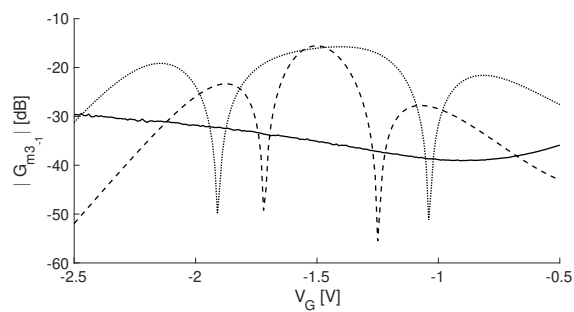
(c) $G_{m3_{-1}}$ versus V_G for PLO=-8 dBm (dashed), PLO=4 dBm (dotted) and PLO=15 (solid)

Figure 4.2: Behavior evolution for parameters responsible for the third-order intermodulation, for different local oscillator power levels at Vds = 8 V.

is shown in Fig. 4.3. The parameter does not decrease as does IMP3 because the shape of $g_m(V_G)$ (cf. Fig. 4.3a) has a larger linear region than that of $g_{m3}(V_G)$ (cf. Fig. 4.2a). On the other hand, the behaviors shown in Fig. 4.3 are consistent with the general trend of the IF component across V_G of Fig. 3.2. From its shape we can see that it increases together with a greater flatness, over a wider range of bias for a PLO level of 15 dBm than for the one for -8 dBm.
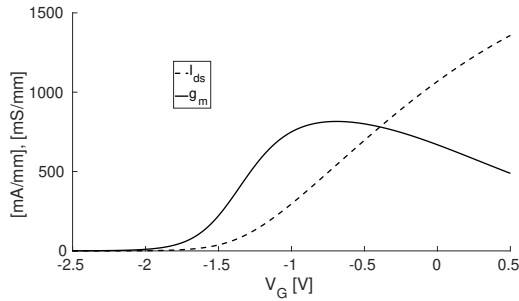
(a) Transconductance g_m.
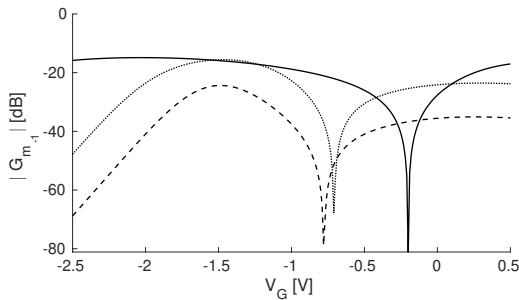
(b) $G_{m_{-1}}$ versus PLO levels: -8 dBm (dashed), 4 dBm (dotted) and 15 dBm (solid)

Figure 4.3: Behavior evolution for parameters responsible for the conversion gain, across V_G, and for different local oscillator power levels at Vds = 8 V.

Repeating the above analysis about the terms $G_{m_{-1}}$ and $G_{m3_{-1}}$ versus the drain voltage V_D, we can observe a general increment of $G_{m_{-1}}$, and a reduction of $G_{m3_{-1}}$, as PLO increases. Thus focusing our interest on PLO = 15 dBm we derived the behavior shown in Fig. 4.4. From the curves we recognize a rather flat behavior above 2 Volt, while sharply roll-off to zero

as V_D approaches zero. This should not be surprising, because this analysis corresponds to an active mixer with the RF signal applied to the gate, and thus significantly different from a resistive mixer topology. The analysis thus justifies the adoption of a drain bias in excess of 5 V, and following a conservative approach we came to the conclusion to adopt 8 V as bias voltage.
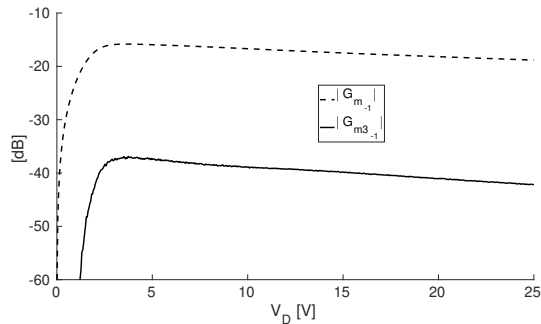

Figure 4.4: Analysis of $G_{m_{-1}}$ and $G_{m3_{-1}}$ versus drain voltage at PLO = 15 dBm, and Vgs = -1.5 V.

This conclusion motivates the development of a balanced mixer capable to deal with a high PLO level in order to minimize the generation of the IMP3, which can be seen as false targets in radar applications.

4.3 MMIC Double-balanced GaN-based gate-pumped mixer

4.3.1 Design

The IMP3 analysis carried out in 3 motivated the development of the GaN-HEMT based gate-pumped active linear mixer, which provides reduced conversion losses, or even a conversion gain, while the injection of a large PLO level, provides very low IMP3. A balanced architecture can effectively cancel the residual second-order IMPs, thus leading to a highly linear active mixer architecture suitable for radar applications. The block diagram of the balanced active mixer is shown in Fig. 4.5; it consists of a pair of gate-pumped active mixers LO driven by a balun, while the RF signal is fed by a 3-dB
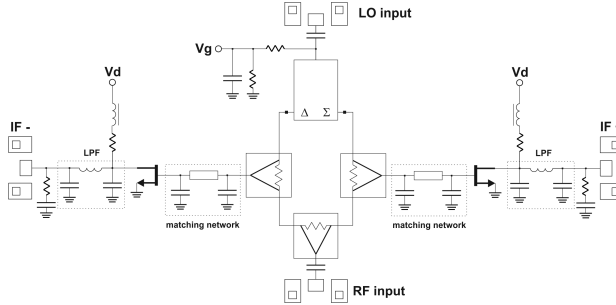
Figure 4.5: Schematic diagram of the balanced active mixer

splitter. In this design, the balun is implemented by a pair of balanced Lange couplers, thus forming a Marchand topology.

This topology ensures the LO - RF isolation, due to the combined functions of the LO balun and the RF splitter. A typical value of RF to LO and LO to RF isolation in excess of 35 dB is expected.

Two additional 3-dB splitters combine the LO and RF signals to both the device gate terminals. A low-Q pi-network at the gate terminal matches the LO and RF signals in the design frequency band, [70], at the design mixer input PLO level of 24 dBm.

The second lumped network implemented in the active mixer consists on a pi-network low-pass filter, whose tasks are multifold. The first is to provide a short circuit at the drain terminal at the LO frequency, this is important as explained in Section 3.2.1 because it permits canceling the drain–source conductance modulation and reducing the feedback from the device output terminal to input, thus significantly reducing the IMPs. The dynamic load line is shown in Fig. 4.6, superimposed on the static I/V characteristics, where we can observe that $i_d(t)$ versus $v_{ds}(t)$ develops mainly in the vertical direction, and where the main dynamic effect is due to the LO signal while a minor variation is expected from the RF signal. The same figure also shows the dynamics at the gate terminal, where the drain current is plotted versus v_{gs}; in this latter case the design should avoid the forward bias of the gate-to-source junction for the sake of reliability. In addition, the network should provide a low-pass transfer function and thus remove the residual LO and RF signals, in this implementation it is of the third order achieved by lumped elements. The filter also embeds a 50 Ω termination and provide DC-coupling with the output terminal. This latter is for the purpose of detecting

very low IF frequencies resulting from short-range radar applications.

In accordance with the assumptions of Section 3.2.1, the IF load is re-
alized by a 20 Ω resistance, and is included in the drain bias line. This
value is a trade-off between the requirement already discussed and the mixer
gain, which turns out to be inversely dependent on the termination. Fi-
nally, a $R = 10$ Ω shunt resistor is inserted at the mixer input, this provides
DC-coupled IF termination and controls the input referred noise voltage.
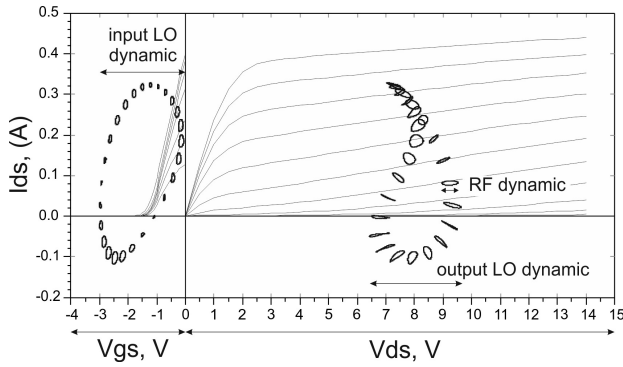
Figure 4.6: Output and input trajectories, i_d vs v_d and v_g, superimposed on
the static I/V characteristics; PLO = 24 dBm at 37.5 GHz, RF power level
-10 dBm and IF frequency 10 MHz.

4.3.2   MMIC Prototype of the proposed mixer

The OMMIC HEMT GaN-on-Si 100 nm process (D01GH) was adopted for
the development of the mixer. In addition to the data provided in Table 3.1,
the device technology features a maximum oscillation frequency of 180 GHz,
a breakdown gate-drain voltage of 36 V, a transconductance of 800 mS/mm,
a noise figure of 1.5 dB at 40 GHz.

A photograph of the MMIC prototype is shown in Fig. 4.7.

The drain bias voltage is 8 V with 20 mA of quiescent current, the DC
current absorption reaches 160 mA with the PLO level set to 25 dBm and
RF power level at 10 dBm.

Figure 4.7: Photograph of the balanced mixer prototype chip

4.4 Experimental Validation

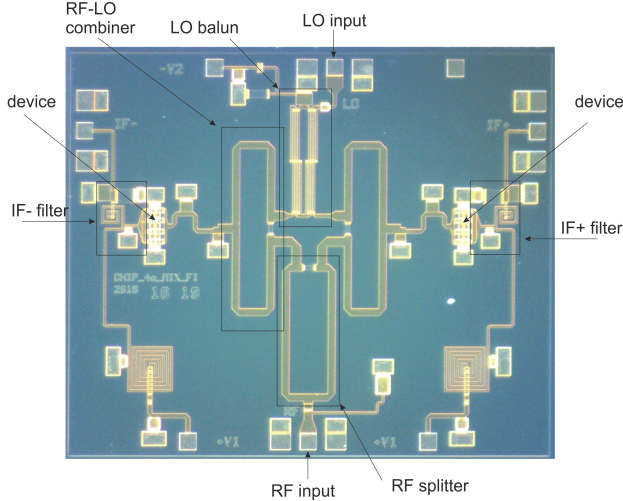In this section we present the characterization data of the prototype described in Section 4.3.2. It consists of calibrated broadband measurements of the large signal two-tone single-ended and balanced performance and the emulation of the radar mode.

4.4.1 Single tone broadband characterization

The first set of data concerns the measured conversion gain in differential mode, defined as $CG = mag(IF^+ - IF^-)/mag(RF)$, within the design frequency band and for a constant IF of 10 MHz. The CG data are presented in Fig. 4.8, along with the effective PLO level driving the LO port of the mixer and the simulated response. Although the PLO level is significantly lower than the nominal one (i.e. 24 dBm), because of the limitations imposed by the source of the vector analyzer, it provides significant information about the broad band capability of the mixer. From the data we can observe a maximum gain of -3 dB, which reduces proportionally with the LO power. The simulated CG, reproduced at the same LO injection levels across the band, provided comparable data as shown in the graph. In addition, according to the graphs in Fig. 4.3b, which show the term $G_{m_{-1}}$ responsible for

the CG, we can observe that about the pinch-off the CG remain constant for PLO levels in excess of 4 dBm. Thus it is to be expected that a maximum conversion loss of about CG$= -4$ dB would be the one at the nominal LO level; an expectation confirmed in Section 4.4.2.

About the RF to LO and LO to RF isolation, it was estimated by measurements in excess of 38 dB at the RF and LO ports across the bandwidth.
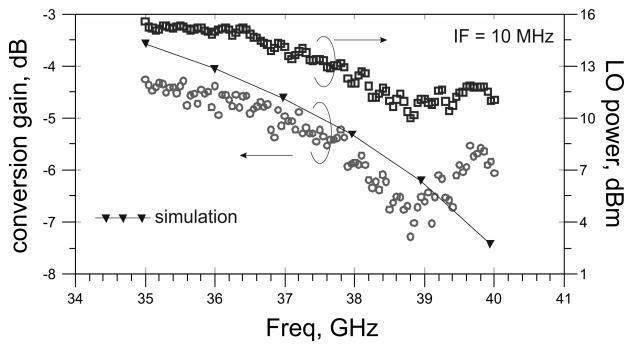

Figure 4.8: Measured CG with calibrated 4-port VNA operating in mixer vector mode (left y-axis) and corresponding actual LO power (right y-axis) versus frequency; simulated CG shown for the same LO power.

4.4.2   Two-tone characterization

Fig. 4.9 presents the measured data in single-ended configuration.

For this purpose, a signal source with sweeping power was connected to the mixer RF port, a second source of 24 dBm nominal power was connected to the LO port, while the IF^+ was connected to a spectrum analyzer; at this stage of the characterization, the port IF^- was 50 Ω terminated. The frequencies of analysis are such that the LO and RF swept in the range 35–40 GHz, keeping constant the IF center at 2.6 MHz, with the two RF tones spaced by $\Delta IF = 1$ MHz.

The experimental data are presented in Figs. 4.9a and 4.9b, along with the corresponding simulated data for LO frequency at 35 GHz, and $\Delta IF = 1$ MHz. The two figures show the same converted data for the sake of a better comparison with the IMPs and to allow the estimation of the intercept points. As the first consideration, we can estimate the second-order input intercept
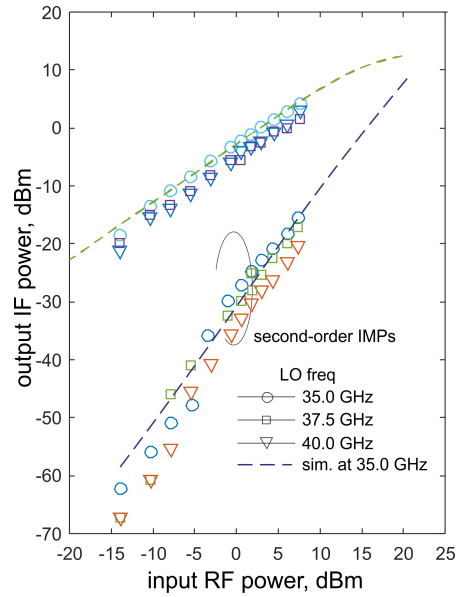
(a) IMP2 and down-conv. signals
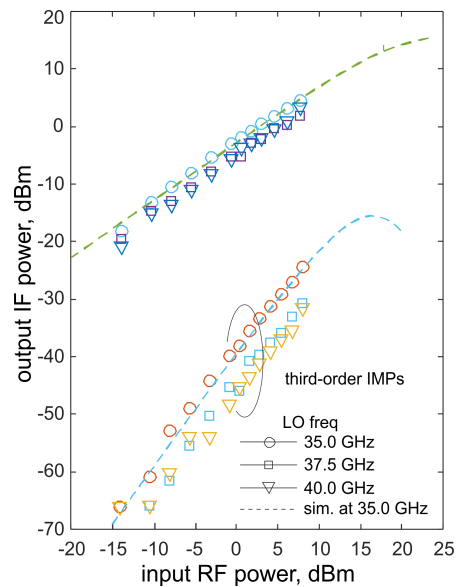
(b) IMP3 and down-conv. signals

Figure 4.9: Two-tone test at LO frequencies of 35, 37.5 and 40 GHz, power 24 dBm. Signals were measured at IF+, for center IF = 2.6 MHz, and RF two-tones offset $\Delta IF = 1$ MHz.

points to be IIP2 = 28.2 dBm, while the third-order input intercept points are IIP3 = 39.1 dBm at 37.5 GHz. The simulated data provides very accurate estimations of both the conversion gain and the intercept points.

The conversion gain at 37.5 GHz from the data turns out to be a value of -5.0 dB which is consistent with that measured by the calibrated VNA and shown in Fig. 4.8.

(a) IF+ port

(b) IF- port

(c) Difference between signals acquired from IF- and IF+ ports.
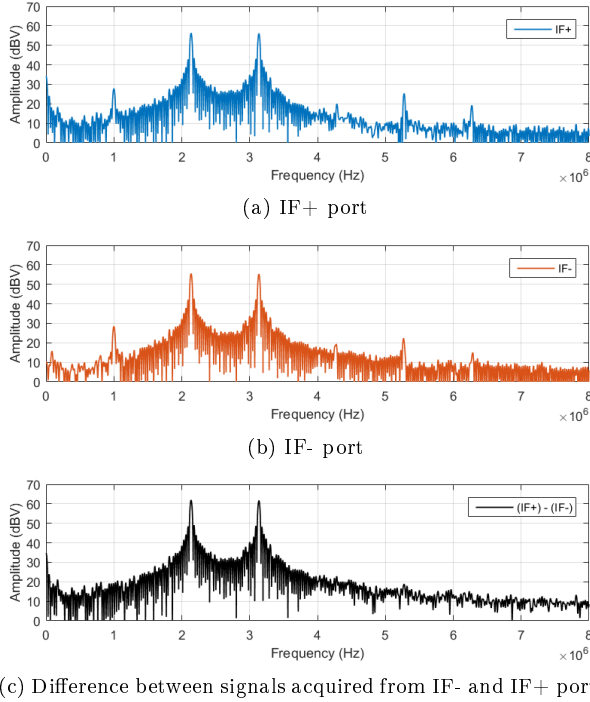
Figure 4.10: Signal spectra IF+ and IF-, acquired by a digital oscilloscope. RF = (37.5026 ± 0.0005) GHz, LO = 37.5 GHz; LO: 24 dBm, RF: 8 dBm

Some insight into the two channel balance and its effectiveness for the cancellation of even-order IMPs will now be discussed. In fact, the two tone test permits verifying the effective balance between IF^- and IF^+ and the ability of the proposed architecture to provide a highly linear mixer performance, by canceling the residual IMPs not minimized by the operation of the active mixer when driven by a large PLO. Considering the case of two tones at RF1=37.5021 GHz and RF2=37.5031, with LO = 37.5 GHz and

Table 4.1: Performance summary versus frequency two-tone test, $IF = IF^{-} - IF^{+}$; with PLO = 24 dBm, IF= 2.5 MHz and referred to IMPs $RF1 - RF2 = 1$ MHz and $2RF2 - RF1 - LO = 1.1$ MHz

frequency (GHz)	35.0	37.5	40.0
CG (dB)	-4.1	-5.0	-5.2
P-1dBm[1]	18.1	17.0	17.2
IIP2 (dBm)	37.6	38.2	39.4
IIP3 (dBm)	38.7	39.1	39.8

[1]P-1dBm is estimated.

RF power level of 8 dBm for each tone, and LO power of 24 dBm, Fig. 4.10 presents the spectra of the two IF outputs acquired by a two channel scope. It is worth noting that the two spectra exhibit a significant amount of IMPs, cf. Figs. 4.10a–4.10b, namely, they are: $RF1 - RF2 = 1$ MHz, $2RF2 - 2LO = 4.2$ MHz, $RF1 + RF2 - LO = 5.2$ MHz, and $2RF2 - 2LO = 6.2$ MHz. All the previous listed even order IMPs become negligible by taking the difference between the two traces, $IF^{-} - IF^{+}$, as shown in Fig. 4.10c. From the same figure we observe that the third order IMPs, namely $2RF2 - RF1 - LO = 1.1$ MHz and $2RF1 - RF2 - LO = 4.1$ MHz, are both below the noise.

A summary of the two tone test characterization, considering the two combined IF signals, is presented in Table 4.1 with respect to the IMPs $RF1 - RF2 = 1$ MHz and $2RF2 - RF1 - LO = 1.1$ MHz.

4.4.3　Radar operating mode

A final test considered the mixer in actual radar set-up mode. For this purpose a 5 dBm linearly swept signal with 1.5 GHz of bandwidth was generated about 37.5 GHz, the ramp-up time was 4 ms, while the ramp-down duration was set at 10 ms. This generated chirp signal was split and sent to both the LO and RF ports, the first through a power amplifier capable of driving the mixer at 24 dBm, while the RF port was fed through a delay line, cf. Fig. 4.11. The delay line introduces 20 dB of losses and 4 ns of delay. The result of the characterization is shown in Fig. 4.12a, where the chirp envelope and the resulting IF signals are shown. In particular, the two individual traces IF^{-} and IF^{+} and their combination ($IF^{-} - IF^{+}$) are also shown.

From the figure we can clearly recognize the change of the IF frequency in correspondence with the ramping-up and the ramping-down envelope and the cancellation of the common mode signal. Fig. 4.12b shows the IF signal in the frequency domain, by which we can observe the almost negligible presence of spurious signals.
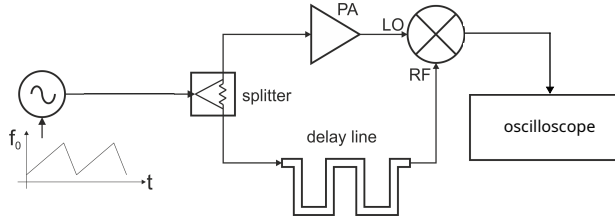
Figure 4.11: Measurement set-up with chirp signal emulating the radar mode.

Table 4.2: Performance summary of reported HEMT GaN mixers

REF	RF(GHz)	Topology	CG(dB)	P_{1dB}(dBm)	$IIP3$(dBm)	$IIP3$-P_{LO}(dB)
[9]	26-31	s.e. resistive	-11	11	22	12
[10]	26-40	bal. resistive	-9	15	28	20
[71]	32-50	s.e. resistive	$-11^{(3)}$	$8.5^{(3)}$	-	-
[17]	26-30	s.e. resistive	-11	10	$20^{(1)}$	10
[72]	75-81	s.e. active	-7.5	13	-	-
[73]	2-4.8	bal. Gilbert	9.3	-5	-	-
[74]	1.55-1.9	s.e. resistive	-9.5	11	27	13
[75]	3.2-5.1	diode pair	-15.3	7	17	5.6
[76]	6-18	s.e. resistive	-10.5	-	$30^{(1)}$	-
[77]	10-12	s.e. resistive	-7	-	30	7
[78]	13.75-14.5	diode pair$^{(2)}$	-25.4	4.8	-	-
[79]	3-40	bal. resistive	-7	22	$32^{(1)}$	5
t.w.	35-40	bal. active	-5.0	$17.0^{(1)}$	39.1	15.1

[1] estimated; [2]single side-band (SSB) subharmonically pumped (SHP); [3] in down-conv.
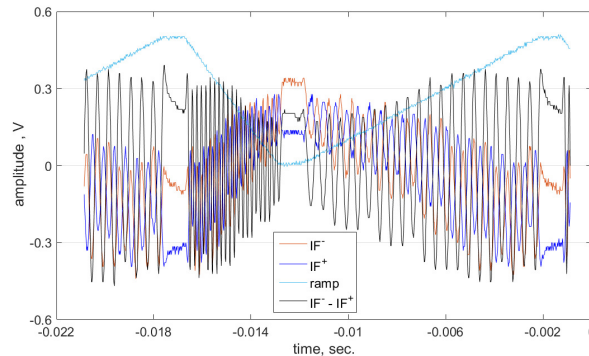
(a) IF^+ and IF^- signals acquired by oscilloscope, their difference $IF^+ - IF^-$, and modulating ramp signal for chirp generation.
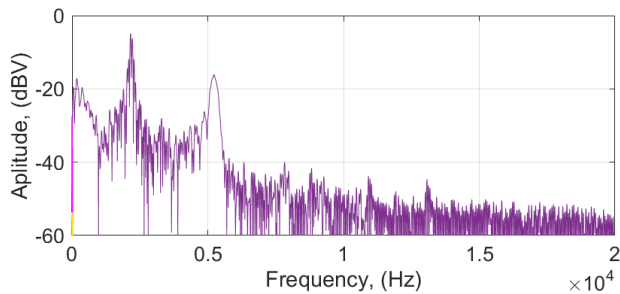
(b) Spectrum of the difference between output IF signals, $IF^+ - IF^-$

Figure 4.12: Experimental results emulating the radar operation mode, by the set-up of Fig. 4.11

4.5   Conclusions

The present work has introduced an active balanced mixer operating in Ka-band developed in GaN-on-Si monolithic microwave integrated circuit technology. A prototype of the mixer was extensively characterized in broadband single- and two-tone tests across the 35–40 GHz band. With a PLO of 24 dBm at 37.5 GHz, it has exhibited a down conversion maximum conversion gain of - 5.0 dB, a second-order input intercept point of 38.2 dBm, and an third-order input intercept point of 39.1 dBm, at IF = 2.5 MHz .

In the recent literature, the development of GaN HEMT-based mixers has been addressed, mostly adopting a resistive topology, with a few realizations adopting active topologies. A comparison between the results introduced by this work and the corresponding state of the art was presented in Table 4.2. From the data we can observe that the proposed mixer outperforms the previously reported data in terms of its linearity and conversion gain, while the work presented in [10] exhibits the highest linearity efficiency.

Chapter 5

A highly-linear GaN SMPA for wireless communications

In this chapter, a nonlinear analysis of a GaN HEMT SMPA based on the time-varying power series approach is presented. For this purpose, the SMPA operation is described as a drain mixer, in which the envelope signal plays the role of the local oscillator. The proposed analysis predicts the internal cancellation of intermodulation products, determined by nonlinear contributions occurring in the SMPA and identifies the responsible terms. The approach is based on the extraction of the requested parameters from dynamic I/V characteristics. This analysis is validated experimentally by a GaN HEMT SMPA operating at 3.8 GHz developed for this purpose, reporting a decrease of third-order intermodulation products in excess of 30 dB. [1]

5.1 Introduction

In modern wireless communication systems, the high peak to average ratio exhibited by digital modulation techniques, forces the PA to operate in back-off regions, with consequent poor efficiency performance. Techniques such as load-modulation and supply-modulation have been widely implemented to

---

[1]This chapter was presented as "A Mixer-Like Nonlinear Analysis for GaN HEMT Supply-Modulated Power Amplifier at 3.8 GHz" at the *17th European Microwave Integrated Circuits Conference (EuMIC)* [57].
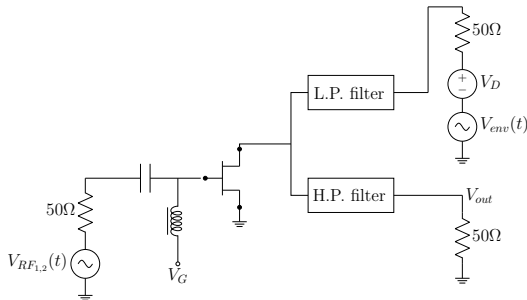
Figure 5.1: Conceptual schematic of SMPA as three-port device.

overcome this problem. This work focuses on the supply-modulation technique applied to PA (SMPA), for which the linearity behavior has been matter of discussion in the last decade [80–86]. Since then, it was demonstrated that the supply modulation has to be treated as a dynamic signal [87], the idea to describe SMPA behavior as a mixer-like operation has been introduced and discussed [30, 88]. Starting from this assumption, a simplified version of the small-signal/large-signal method, that is a canonical tool for the mixers [18, 31, 54, 70], is applied to SMPA analysis. This method models the strongly-nonlinear circuit as a weakly-nonlinear system in which the effect of the large signal are modeled as a modulation of the Taylor-series expansion coefficients of the device drain current. Unlike harmonic-balance algorithm, this method allows to details the inter-modulation distortion process within the device and, as a consequence take into account the most important nonlinear contributions. Furthermore, it is widely known that this approach is able to get accurate predictions on field-effect transistors IMPs but at the cost of a considerable effort for the preliminary device parameters extraction [32].

In this work, we show that the method is able both to get predictions of the internal cancellation occurring in SMPAs, and to evaluate the single responsible terms with the only knowledge of the device I/V curves.

5.2   Analysis

5.2.1   The SMPA mixer-like operation

Starting from the assumption that an SMPA can be modeled as a three-port mixer like device, this leads to describe the low-frequency supply modulation as a V_{env} signal, while the amplifier input and output signals are associated to the V_{RF} and V_{out} respectively. In this work an SMPA with a two-tone input signal $V_{RF_{1,2}}$ of frequency ω_1, ω_2 and the supply modulation V_{env} at the third port is considered, as shown in figure 5.1. By considering the input signal as a modulated signal

$$
\begin{aligned}
V_{RF_{1,2}}(t) &= k(cos(\omega_1 t) + cos(\omega_2 t)) \\
&= 2kcos(\frac{\omega_2 - \omega_1}{2}t)cos(\frac{\omega_2 + \omega_1}{2}t),
\end{aligned} \tag{5.1}
$$

where k is the amplitude of each tone, it is known that by injecting a V_{env} signal of frequency $(\omega_2 - \omega_1)/2$ the effect is the maximization of the amplifier efficiency and as a consequence, the behavior is that of an envelope-tracking power amplifier. Similarly it was observed that injecting a signal at $\omega_2 - \omega_1$ the results can be an improvement in SMPA linearity by means of a destructive interactions with the third-order inter-modulation distortion tone at the frequency $2\omega_2 - \omega_1$ internally generated.

We hereby, derive a simplified version of the small-signal/large-signal analysis to predict the occurrence of the internal cancellation in an SMPA.

In this three-port scenario, the assignment of the large-signal role to the supply-modulation leads the SMPA to be viewed as a drain mixer, with a drain bias V_D, such as to operate in a region of flatness I/V output characteristics. It is worth noting that the low-frequency characteristic of the V_{env} signal, prevents its leakage towards the gate terminal, providing an effect similar to that of the well known local-oscillator short-circuit at the gate side of the drain-mixer. As it is demonstrated hereinafter, this choice shows positive effects also in terms of efficiency.

5.2.2   Pseudo drain-mixer intermodulation products

In such operating conditions the most important nonlinear contribution to the IMPs, of our pseudo drain-mixer is the device trans-conductance. Since the aim of the work is to demonstrate the ability of the proposed technique to predict the occurrence of nonlinear phenomena with the only knowledge
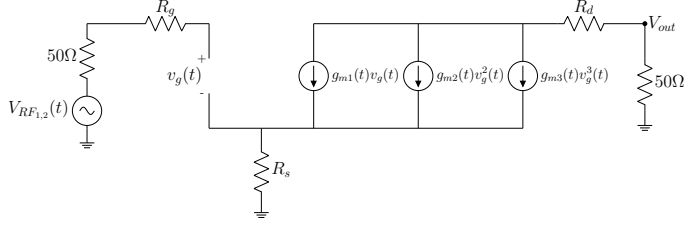
Figure 5.2: Equivalent circuit of the schematic depicted in 5.2 for the time-varying power series analysis. The third port has been omitted since its effect is modeled by the time-varying transconductances.

of the device I/V characteristics, the intrinsic reactive components have been neglected. From the equivalent circuit of Fig. 5.2, the output drain current can thus be written as

$$i_d(t) \approx g_{m1}(t)v_g(t) + g_{m2}(t)v_g^2(t) + g_{m3}(t)v_g^3(t) \tag{5.2}$$

where $g_{m1}(t)$, $g_{m2}(t)$ and $g_{m3}(t)$ are time-dependent, since they are modulated by the V_{env} signal. We have to reformulate (5.2) in the domain frequency to make evident the fundamental harmonics at ω_1, ω_2 and the third-order ones at $2\omega_1 - \omega_2, 2\omega_2 - \omega_1$. For simplicity, we show the analysis only for the right side of the output spectrum since the procedure is identical. By rewriting (5.2) in frequency domain and using the matrix form of the convolution product, we obtain

$$\mathbf{I_d} \approx \mathbf{G_{m1}V_g} + \mathbf{G_{m2}V_g^{(2)}} + \mathbf{G_{m3}V_g^{(3)}}, \tag{5.3}$$

where $\mathbf{G_{m1}}$, $\mathbf{G_{m2}}$, $\mathbf{G_{m3}}$ represent the conversion matrices and $\mathbf{V_g}$, $\mathbf{V_g^{(2)}}$ and $\mathbf{V_g^{(3)}}$ the matrices of phasors of the $v_g(t)$ signal [31]. The components of $\mathbf{I_d}$ at ω_2 and $2\omega_2 - \omega_1$ are respectively

$$\begin{aligned} I_d(\omega_2) &\approx G_{m1_0}V_g(\omega_2) + G_{m1_1}V_g(\omega_1) \\ &+ G_{m3_1}V_g^{(3)}(\omega_1) + G_{m3_2}V_g^{(3)}(2\omega_1 - \omega_2) \end{aligned} \tag{5.4}$$

and

$$\begin{aligned} I_d(2\omega_2 - \omega_1) &\approx G_{m3_0}V_g^{(3)}(2\omega_2 - \omega_1) \\ &+ G_{m1_1}V_g(\omega_2) + G_{m3_1}V_g^{(3)}(\omega_2) \\ &+ G_{m1_2}V_g(\omega_1) + G_{m3_2}V_g^{(3)}(\omega_1) \end{aligned} \tag{5.5}$$

where $G_{m\alpha_k}$ is the component of the $\mathbf{G_{m\alpha}}$ conversion matrix corresponding to the k-th Fourier coefficient of the $g_{m\alpha}(t)$ waveform. In both the (5.4) and in the (5.5), it is possible to identify the terms whose contribution is mostly due to the static bias V_D, that can be approximated with the ones with the subscript $k = 0$, from those due to the presence of V_{env}, which are termed by $k \neq 0$. We can thus write (5.5) as

$$I_d(2\omega_2 - \omega_1) \approx I_{d_{amp}}(2\omega_2 - \omega_1) + I_{d_{env}}(2\omega_2 - \omega_1) \qquad (5.6)$$

In (5.6) we recognize the sum of two contributions, being the first generated internally while the second induced by the dynamic supply.

5.2.3 Conversion matrices extraction

The implementation of (5.4) and (5.5) requires the extraction of the conversion matrices. From the same equations we note that the second order conversion matrix does not contribute to the terms of our interest, thus it can be neglected. In order to extract the conversion matrix an automated procedure was implemented. The measures were carried out on a test circuit containing the stand-alone device with a proper set of bias-T. For this task the device under characterization is the Cree GaN HEMT CGH60004S .

Firstly the drain bias-dependent transconductance and its derivatives have been extracted, while the bias voltage was kept fixed where the transconductance peaks, about $-1.6\,\text{V}$. This extraction procedure is dynamic as to avoid traps and self-heating effects and follows the one explained in [59]. A low-frequency tone has been injected in the single device and the power of the first and third harmonics has been measured for different drain-bias values. The application of the nonlinear current method then leads to the extraction of $g_{m1}(V_D)$ and $g_{m3}(V_D)$ reported in Fig. 5.3. Knowing $V_{env}(t)$, the evaluation of $g_{m1}(t)$, $g_{m3}(t)$ and thus of $\mathbf{G_{m1}}$, $\mathbf{G_{m3}}$ is straightforward.

5.2.4 Analysis results

The Fig. 5.4 shows a contour plot reporting the values of the $P(2\omega_2 - \omega_1)$ as function of V_{env} magnitude and V_{RF2} phase. The plot reveals the presence of a minimum, for V_{env} magnitude of about 8.3V and V_{RF2} phase value of 63°. The V_D is set at 20V.

The Fig 5.5 shows the contributions of $P_{amp}(2\omega_2 - \omega_1)$ and $P_{env}(2\omega_2 - \omega_1)$ in relation with $P(2\omega_2 - \omega_1)$. When the cancellation occurs, $P(2\omega_2 - \omega_1)$
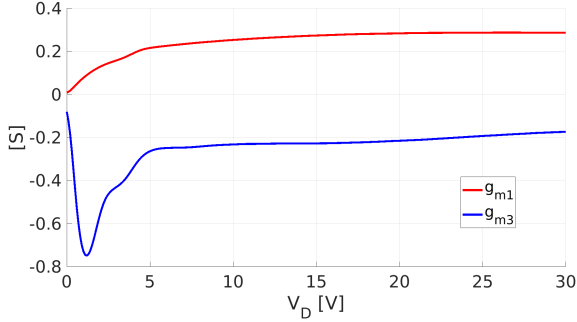
Figure 5.3: Extracted $g_{m1}(V_D)$ and $g_{m3}(V_D)$

decreases of more than 30 dB with respect of the non applied V_{env} condition. The cancellation is confirmed by the polar plot of Fig. 5.6, in which the two contributions $I_{d_{amp}}$ and $I_{d_{env}}$ show to have opposite phase and equal magnitude when the V_{RF_2} input phase is 63° and the V_{env} magnitude is 8.3 V.

The analysis results also report that, as might be guessed, the minimum occurs for different V_{env} if the input power varies. In fact, if the input power increases the minimum occurs for higher V_{env} and vice-versa. It is worth to mention that being the V_{env} limited up to 10 Vpp (instrumentation limit), the applied input power was the maximum one for which the cancellation still occurs and the shape of the intermodulation is appreciable. Both the analysis and the measurement were performed following this criterion.

5.3   Experimental results

5.3.1   SMPA fabrication and measurements

An SMPA operating in 3.4 ÷ 3.8 GHz based on the same characterized device in the extraction procedure was designed, fabricated and characterized. The picture of the developed SMPA prototype is shown in Fig. 5.7. The measurements setup aimed at the search of the inter-modulation minimum is illustrated in Fig. 5.8. The setup involves the use of an driver amplifier, along with arbitrary waveform generators for both the synthesis for the two tone input signal, with arbitrary phase relations, and the envelope signal of arbitrary amplitude.
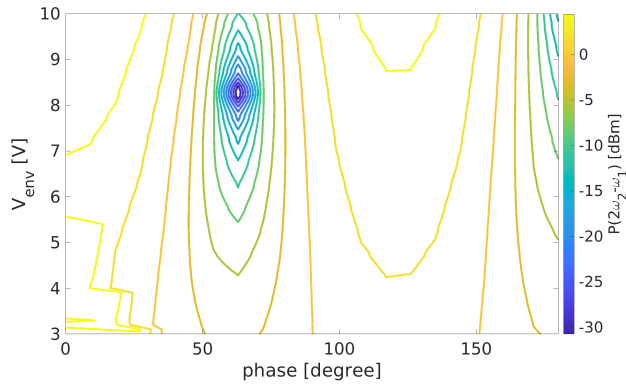
Figure 5.4: Third-order IMPs $P(2\omega_2 - \omega_1)$ in dBm as function of the phase of the input signal V_{RF_2} and the V_{env}. We can see the minimum occurring for $V_{env} = 8.3$V and $phase = 63°$.
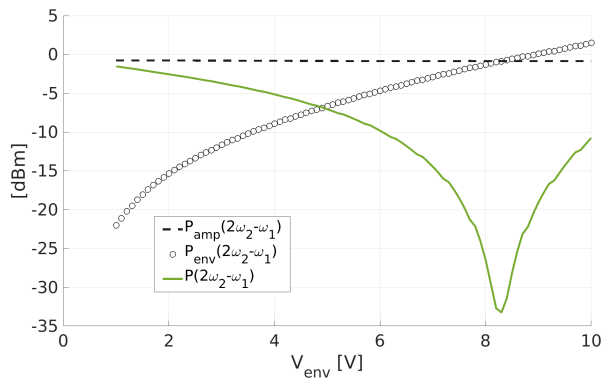

Figure 5.5: $P_{amp}(2\omega_2-\omega_1)$, $P_{env}(2\omega_2-\omega_1)$ and their composition $P(2\omega_2-\omega_1)$ as function of V_{env} for $phase = 63°$.
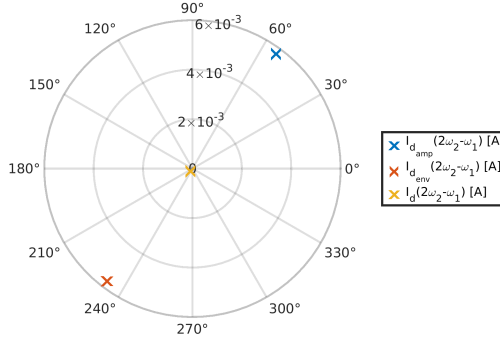
Figure 5.6: $I_{d_{amp}}(2\omega_2 - \omega_1)$, $I_{d_{env}}(2\omega_2 - \omega_1)$ and their sum $I_d(2\omega_2 - \omega_1)$ for $V_{env} = 8.3$V and $phase = 63°$.

A two tone signal of frequency 3.8 ± 0.02 GHz and power 15 dBm were injected in the input. A supply modulation signal of 40 MHz was applied at the third port, and its amplitude varied between 1 Vpp and 10 Vpp around a DC value of 20 V. The gate bias was kept fixed at the same value as of the analysis, that is -1.6 V; the output power measurements have been performed on a digital spectrum analyzer. Fig. 5.9 shows the comparison between the analysis results at V_{RF_2} phase of $63°$ and the experimental results. In the experimental data, the minimum occurs with the phase of V_{RF_2} tone of $10°$, with the $P(2\omega_2 - \omega_1)$ drops of about 30 dB, as in the analysis result. From the comparison we observe that, despite its simplicity, the analysis is able to make a good prediction of the trends of both the fundamental $P(\omega_2)$ and third-order IMPs $P(2\omega_2 - \omega_1)$ as well as of the intermodulation cancellation occurrence.

This makes the analysis a valuable tool in the design stage of SMPAs, and overall explain the cancellation mechanism occurring in a SMPA for the cancellation of the IMP by using a proper bias envelope.

5.3.2 Drain efficiency measurements

Due to the limitations of the envelope generator, that was able to provide up to 10 Vpp, the input power was limited up to 18 dBm for the cancellation to occur. For such input power level, setting V_D bias level at 20 V, the envelope signal produces a negligible effect on the SMPA efficiency.
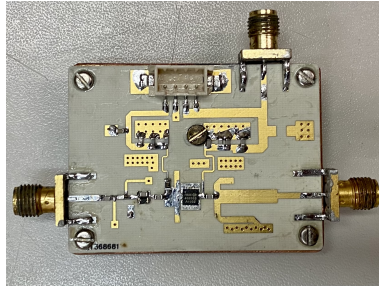
Figure 5.7: Picture of the fabricated SMPA.
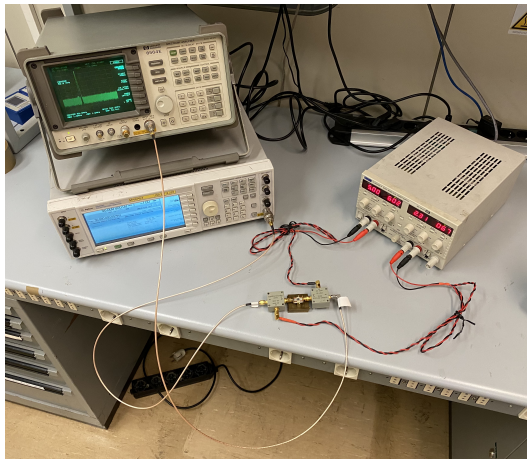
Figure 5.8: Setup for the third-order IMPs measurements of the proposed SMPA.
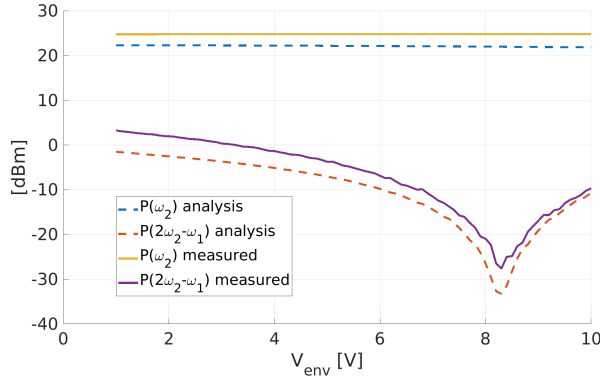
Figure 5.9: Comparison between analysis and measured results of fundamental and third-order IMPs.

In order to overcame the drawbacks related with the generator dynamics the drain bias V_D was lowered from 20 V to 10 V with the aim to maximize the effect of the envelope tone on the amplifier efficiency. The results are showed in Fig. 5.10, from which we can observe that the phase value corresponding to the third-order IMPs minimum also allows an excellent trend for the drain efficiency, that reaches values near 75 %.
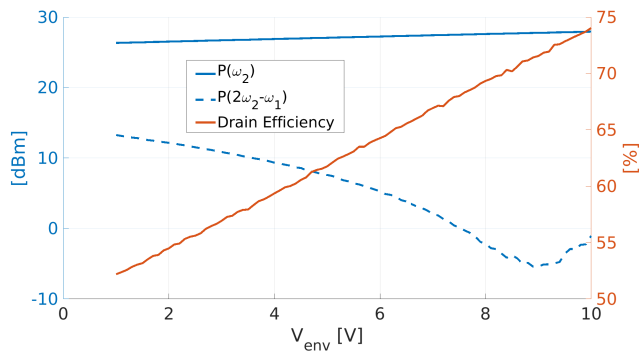
Figure 5.10: SMPA efficiency improvement in intermodulation suppression condition.

5.4   Conclusion

A nonlinear analysis for SMPAs based on a mixer-like modeling has been presented. Its ability to predict the occurrence of internal cancellations and to identify the responsible terms has been demonstrated on a fabricated SMPA operating in S-band. The SMPA showed a drop of third-order IMPs of about $30\,\mathrm{dB}$ as predicted by the analysis. A measurement of the drain efficiency when the minimum occurs was also reported, showing values near $75\,\%$.

Chapter 6

Conclusion

6.1 Summary of contribution

The main scientific contribution of the thesis is the demonstration that the GaN technology opens new frontiers of linearity for active mixers and SM-PAs. The contributions are specified in the following, in order of appearance in the thesis. First, the positive impact of the GaN technology on the drain-pumped mixer conversion gain and linearity. The mixer exhibited both the highest conversion gain and the highest IIP3 of $+10\,\mathrm{dB}$ and $+11\,\mathrm{dBm}$, respectively, among the same class of mixers reported in the literature. Second, the prove that, in GaN-based gate-pumped mixers, the device output-conductance doesn't influence almost at all the overall mixer operation. Third, the experimental-based comparison between GaN and GaAs-based gate-pumped mixers in terms of linearity. This comparison fully justified the use of the GaN technology for the development of a highly-linear gate-pumped mixer. Fourth, the analytical explanation about the relation between the linearity of a gate-pumped mixer and the LO level. Fifth, the development of a mixer exhibiting the IIP3 state-of-the-art in the Ka frequency-band. Sixth, the development of a SMPA exhibiting a decrease of third-order IMPs in excess of $30\,\mathrm{dB}$. Seventh, the prove that a mixer-like approach can be applied for the prediction of nonlinear mechanisms occurring in SMPAs.

6.2   Directions for future work

The demonstration of the GaN technology improving the linearity in active mixers and PAs opens two scenarios. The first concerns a new role for active mixers in radar receivers. Their linearity feature, together with their conversion gain, could suggest their implementation in place of the series composed by low-noise amplifier (LNA) and resistive mixer. Since the modern radar systems require a large number of receiver and transmitter modules, such solution would reduce the system complexity and thus the costs. To be feasible, this solution requires mixers with low noise-figure. For these considerations, the short-term research goes towards minimizing the noise figure of active mixers.

The second, concerning the SMPAs, is related to the application of the linearization technique implemented in this thesis to an actual wireless-communications context. In fact, in this thesis such linearization condition served as a proof-test for the presented nonlinear technique. As such, it was implemented in the academic situation of a two-tone constant-power input signal, being the minimum number of tones able to generate third-order intermodulations products falling within the useful band. Therefore, the short-term research in this context regards the extension of the linearization technique to the case of wide-band variable-power input signals.

Appendix A

Appendix

This appendix concerns a different usage scenario for the time-varying power-series analysis. In particular, it describes the role of the analysis in the improvement of the RF-to-IF isolation in a quad-fet GaAs-based passive-mixer.

A.1 The time-varying power-series analysis: a case-study in the design of a quad-fet passive mixer

In this work we introduced a new architecture of balanced passive mixer aimed at providing very high bandwidth and very high isolation between RF and IF ports. The architecture is based on a double Marchand balun that allows routing the interconnection between the quad-transistors terminals such that the overlaps and misalignment between interconnections are avoided. The operation of the introduced architecture, as well as its influence on the isolation, were described basing on the extraction of the devices time-varying output-conductances. The actual operation of the architecture was then demonstrated by a mixer prototype fully integrated in 0.2 μm GaAs p-HEMT process. The mixer showed an isolation between RF (input) and IF (output) between 36 dB and

42 dB. [1]

A.1.1   Passive quad-FET mixer analysis

The mixer is based on a quad-FET topology, which is quite well diffused due to its linearity capability and its isolation about the LO leakage toward the IF and RF ports, [90]. In this work we focus on the additional requirement about the maximization of the IN-OUT isolation. The analysis consider the extraction of the time varying conductance associated to the single p-HEMT due to the action of the LO signal. The Fig. A.1a reports the representation of the quad-FET in terms of its time-varying conductance in the balanced topology.

In order to enable a qualitative mixer analysis, we make the common approximation for FET resistive mixers that the main nonlinearity is due to the nonlinear conductance g_{ds}, [70].

By modeling the effect of the local oscillator as a g_{ds} modulation, we can write (A.1) as

$$i_d(v_d) \approx g_{ds}(t)v_d + g_{d2}(t)v_d^2 + g_{d3}(t)v_d^3 \qquad (\text{A.1})$$

Considering the mixer at low level injection we can reduce to the only term $g_{ds}(t)$ and in particular we adopt $\hat{g}_{ds}(t) = g_{ds}(t)/max\{g_{ds}(t)\}$. Referring to the circuit schematic in Fig. A.1a, the $\hat{g}_{ds}(t)$ driven by the LO+ and LO- respectively $g_1(t)$ and $g_2(t)$, are reported in the Fig. A.1b. From the picture we see a somehow square waveforms, which are identical and delayed of an half period of the LO (in the case of the figure the LO frequency is 1 GHz), [91]. An experimental characterization of this device can be effectively carried out by large-signal vector measurements, [92]. Again referring to the Fig. A.1a, we can derive the analytical expression of the conversion mechanism in terms of the IF and RF voltage which is function of the $g_i(t)$

$$v_{IF}(t) = v_{RF}(t) \left[\frac{g_1(t) - g_3(t)}{g_1(t) + g_3(t)} - \frac{g_2(t) - g_4(t)}{g_2(t) + g_4(t)} \right] \qquad (\text{A.2})$$

From the (A.2), we can see that in the ideal LO driving case the term in square brackets consist on a somehow square waveform with zero mean value.

---

[1]This work was presented as "A New Architecture of Broadband GaAs MMIC Balanced Mixer for Very High RF/IF Isolation for 0.5-18.5 GHz Signal Analysis" at the *17th European Microwave Integrated Circuits Conference (EuMIC)* [89].

Observing that a zero mean value has no DC component in the Fourier
spectrum, the IF signal does not include the RF frequency. A deviation
from this ideal assumption, in terms of both amplitude and phase, lead to
asymmetries in the $(g_1(t) - g_3(t))$ and $(g_2(t) - g_4(t))$; these are exemplified
in the Fig. A.1c were the LO+ and LO-, were assumed different 1 dB in
term of amplitude, and 5 degree in term of relative phase. Moving back to
(A.2) the symmetry of the LO driving the quad-FET is mandatory to obtain
a zero mean value equivalent conductance and thus isolation between the
input port and output.

This led to the design of a new architecture which is oriented to maximize
the isolation between the input and the output port, while maintaining high
LO isolation to output port and flat behavior in the conversion bandwidth.

(a) Time-varying conduc-
tances
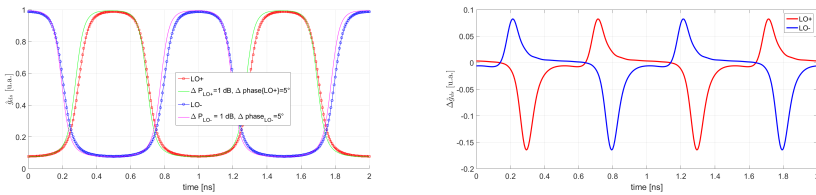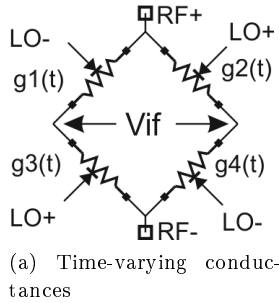
(b) Waveforms of g_ds as function of LO signals(c) time varying difference between g_ds wave-
forms

Figure A.1: Large-signal/small-signal analysis of quad-FET

The designed architecture hereby introduced consists on the dual LO
driving the quad-FET mixer core. In this way the design permits to layout
the p-HEMTs with no intersections of the the gates signal routing and thus
preserve the balance between the large-signal pump at the gates terminal
of the p-HEMTs. Indeed intersection between transmission line driving the

balanced LO signal to two pairs of gates terminals, determines an unavoidable overlap and thus signal integrity degradation. Thus the 4 p-HEMTs can be laid out in a row thus permitting a careful balancing of the two pairs of balanced LO signals. The rest of the circuit is more conventional, it includes a wide band balun for the input signal and a buffer to extract the output signal from the quad-FET without unbalancing the structure.

The Fig. A.2 reports the circuit schematics of the double balanced mixer where the circuit topology of the input active balun and the buffer are reported, along with the specific interconnection between the two identical balun and the quad-FET mixing core.
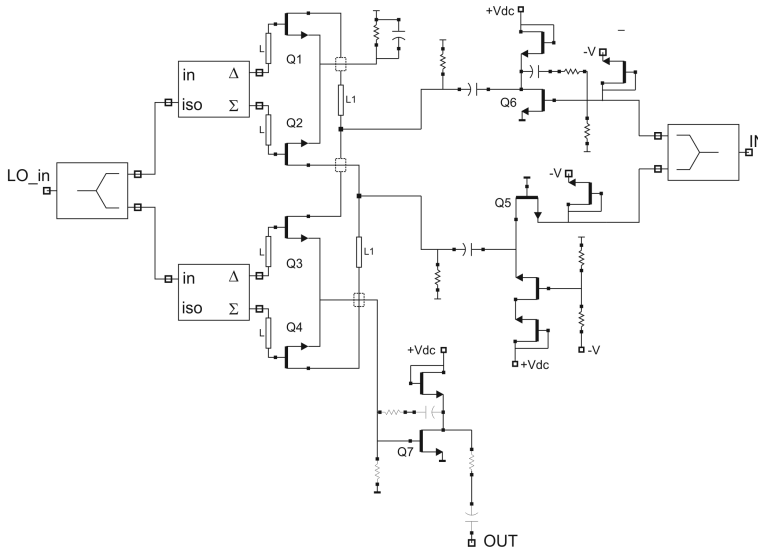
Figure A.2: Schematic of the double balanced mixer.

A.1.2   Experimental Results

The mixer circuit was implemented in the 0.25 μm p-HEMT GaAs PH25 process provided by UMS. The picture of the fabricated IC is shown in Fig. A.3.   The characterization consists in applying the input signal in the the three operative bandwidths, B1, B2, and B3 and for each of the the corresponding LO signal at the frequencies defined in Table A.1, the LO levels was maintained at 10 dBm for each operative bandwidth. The
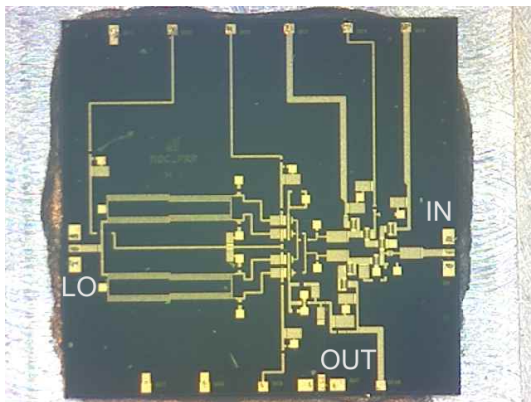
Figure A.3: Photograph of prototype chip.

Table A.1: Mixer operative bandwidths.

O.B.	Input (GHz)	Output (GHz)	LO freq. (GHz)	LO to OUT isol. (dB)
B1	$0.5 - 6.5$	$6 - 12$	12.5	42.5
B2	$6.5 - 12.5$	$6 - 12$	18.5	40.5
B3	$12.5 - 18.5$	$6 - 12$	24.5	39.5

resulting conversion gain is provided in Fig. A.4, across the entire set of
operating frequencies. From the picture we can see that the mixer exhibits
a conversion loss of 5 dB $\pm$ 1.5 dB across the bandwidth. The reduced
losses are attributed to the output buffer that contributes with few dBs of
gain, thus reducing the mixer conversion losses. The prototype exhibited an
isolation between input (RF) and output (IF) port spanning between 36 dB
and 42 dB, while the isolation between LO and output port was between 40
dB and 42.5 dB at the three LO frequencies.

With respect to the state-of-the-art available in literature, the mixer
exhibits the best in its class of mixers RF to IF isolation with associated
highest fractional bandwidth.

Figure A.4: Conversion gain and IN-OUT isolation in the three operative bandwidth defined in Table A.1.

Appendix B

Publications

This research activity has led to several publications in international journals and conferences. These are summarized below.

International Journals

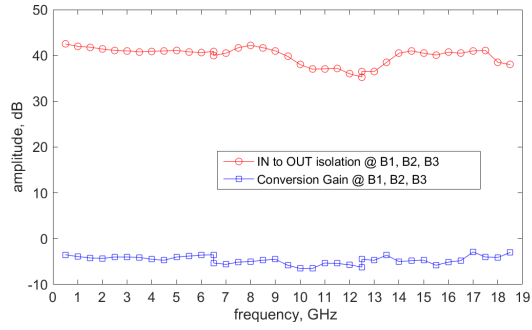1. **Pagnini, L.**; Collodi, G.; Cidronali, A. "A GaN-HEMT Active Drain-Pumped Mixer for S-Band FMCW Radar Front-End Applications", *Sensors*, 2023, 23, 4479. https://doi.org/10.3390/s23094479

2. A. Cidronali, **L. Pagnini**, G. Collodi, and M. Passafiuume, "A highly linear ka-band gan-on-si active balanced mixer for radar applications", *IEEE TRANSACTIONS ON CIRCUITS AND SYSTEMS. I, REGULAR PAPERS*, vol. 69, no. 11, pp. 4453-4464, 2022. [DOI: 10.1109/TCSI.2022.3193960]

3. A. Cidronali, G. Collodi, and **L. Pagnini**, "High-power uhf doherty amplifier output combiner network optimization by 3-port sub- circuit x-parameters characterization", *MICROWAVE AND OPTICAL TECHNOLOGY LETTERS*, vol. 63, no. 2, pp. 404-410, 2021. [DOI: 10.1002/mop.32610]

4. A. Cidronali, G. Collodi, S. Maddio, **L. Pagnini**, M. Passafiume, and G. Pelosi, "A parametric analysis of modified complementary split ring resonator low-pass notch filter suitable for the coexistence of 5.8 ghz dsrc and 5.9 ghz its applications", *PROGRESS IN ELECTROMAGNETICS RESEARCH M*, vol. 108, pp. 17-26, 2022. [DOI: 10.2528/PIERM21121304]

International Conferences and Workshops

1. **L. Pagnini**, G. Collodi, and A. Cidronali, "A mixer-like nonlinear analysis for gan hemt supply-modulated power amplfier at 3.8 ghz", *in proceedings of*

17th European Microwave Integrated Circuits. European Microwave Associ-ation, Milan (Italy), 2022.

2. **L. Pagnini**, G. Collodi, M. Passafiume, and A. Cidronali, "A new architec-ture of broadband gaas mmic balanced mixer for very high rf/if isolation for 0.5-18.5 ghz signal analysis", *in proceedings of 17th Euro- pean Microwave Integrated Circuits. European Microwave Association*, Milan (Italy), 2022.

National Conferences

1. **L. Pagnini**, G. Collodi, A. Cidronali, "Analysis of a Single-Ended GaN-based Drain-Pumped Mixer for Radar Applications", in *Proceedings of 53rd Annual Meeting of the Italian Electronics Society*, Pizzo (Vibo Valentia), Italy, 2022.

Bibliography

[1] R. Clarke and J. W. Palmour, "sic microwave power technologies," *Proceedings of the IEEE*, vol. 90, no. 6, pp. 987–992, 2002.

[2] R. S. Pengelly, s. M. Wood, J. W. MilliGaN, S. T. Sheppard, and W. L. Pribble, "A review of GaN on sic high electron-mobility power transistors and mmics," *IEEE Transactions on Microwave Theory and Techniques*, vol. 60, no. 6, pp. 1764–1783, 2012.

[3] N. Turner, F. L. Pour, and D. S. Ha, "Design of a high temperature 2.37 ghz voltage-controlled oscillator with gan-on-sic hemts," *IEEE Transactions on Circuits and Systems I: Regular Papers*, vol. 67, no. 12, pp. 5153–5161, 2020.

[4] G. R. Nikandish, R. B. Staszewski, and A. Zhu, "Broadband fully integrated gan power amplifier with minimum-inductance bpf matching and two-transistor am-pm compensation," *IEEE Transactions on Circuits and Systems I: Regular Papers*, vol. 67, no. 12, pp. 4211–4223, 2020.

[5] I. Takenaka, K. Ishikura, K. Asano, S. TaKahashi, Y. Murase, Y. Ando, H. TaKahashi, and C. Sasaoka, "High-efficiency and high-power microwave amplifier using GaN-on-Si fet with improved high-temperature operation characteristics," *IEEE Transactions on Microwave Theory and Techniques*, vol. 62, no. 3, pp. 502–512, 2014.

[6] P. Colantonio and R. Giofrè, "A GaN-on-Si mmic power amplifier with 10w output power and 35% efficiency for Ka-band satellite downlink," in *2020 15th European Microwave Integrated Circuits Conference (EuMIC)*. IEEE, 2021, pp. 29–32.

[7] S. Lai, D. Kuylenstierna, M. ozen, M. Horberg, N. Rorsman, I. Angelov, and H. Zirath, "Low phase noise GaN hemt oscillators with excellent figures of merit," *IEEE Microwave and Wireless Components Letters*, vol. 24, no. 6, pp. 412–414, June 2014.

[8] R. Weber, M. Cwiklinski, S. Wagner, R. Lozar, H. Massler, P. Brückner, and R. Quay, "A beyond 110 GHz GaN cascode low-noise amplifier with 20.3 dbm

output power," in *2018 IEEE/MTT-S International Microwave Symposium-IMS*.   IEEE, 2018, pp. 1499–1502.

[9] A. De Padova, P. E. Longhi, S. Colangeli, W. Ciccognani, and E. Limiti, "Design of a GaN-on-Si single-balanced resistive mixer for Ka-band satcom," *IEEE Microwave and Wireless Components Letters*, vol. 29, no. 1, pp. 56–58, 2018.

[10] D. Parveg, M. Varonen, M. Kantanen, and J. Pusa, "A full ka-band highly linear efficient gan-on-si resistive mixer," in *2021 IEEE MTT-S International Microwave Symposium (IMS)*, June 2021, pp. 645–648.

[11] G. Collodi, M. Passafiume, T. Bilotta, and A. Cidronali, "A Ka-band GaN-on-Si mmic analog vectorial modulator and its broadband calibration procedure," *IEEE Microwave and Wireless Components Letters*, vol. 31, no. 4, pp. 377–380, 2021.

[12] H. Mizutani, R. IshiKawa, and K. Honjo, "A novel reconfigurable GaN filter mmic with active reflector," in *2018 Asia-Pacific Microwave Conference (APMC)*.   IEEE, 2018, pp. 717–719.

[13] J. M. Salem, F. L. Pour, and D. S. H. Life, "A high-temperature model for GaN-hemt transistors and its application to resistive mixer design," *IEEE Transactions on Circuits and Systems I: Regular Papers*, vol. 68, no. 2, pp. 581–591, 2020.

[14] J. Hu and K. Ma, "Analysis and design of a broadband receiver front end for 0.1-to-40-ghz application," *IEEE Transactions on Circuits and Systems I: Regular Papers*, vol. 68, no. 6, pp. 2393–2403, 2021.

[15] R. Rieger, A. Klaaben, P. Schuh, and M. Oppermann, "GaN based wideband t/r module for multi-function applications," in *2015 European Microwave Conference (EuMC)*, Sep. 2015, pp. 514–517.

[16] M. S. Clements, A.-V. Pham, J. S. Sacks, B. C. Henderson, and S. E. Avery, "Comparison of highly linear resistive mixers in depletion and enhancement mode gaas and GaN phemts at Ka band," in *2018 IEEE/MTT-S International Microwave Symposium-IMS*.   IEEE, 2018, pp. 435–438.

[17] M. Do, M. Seelmann-Eggebert, R. Quay, D. Langrez, and J. Cazaux, "Al-GaN/GaN mixer mmics, and rf front-end receivers for c-, ku-, and Ka-band space applications," in *The 5th European Microwave Integrated Circuits Conference*.   IEEE, 2010, pp. 57–60.

[18] S. A. Maas, "Two-tone intermodulation in diode mixers," *IEEE transactions on microwave theory and techniques*, vol. 35, no. 3, pp. 307–314, 1987.

[19] J. Zhang, M. Bao, D. Kuylenstierna, S. Lai, and H. Zirath, "Transformer-based broadband high-linearity hbt gm-boosted transconductance mixers,"

IEEE transactions on microwave theory and techniques, vol. 62, no. 1, pp. 92–99, 2013.

[20] J. Hashimoto, K. Itoh, M. Shimozawa, and K. Mizuno, "Fundamental limitations on the output power and the third-order distortion of balanced mixers and even harmonic mixers," *IEEE Transactions on Microwave Theory and Techniques*, vol. 64, no. 9, pp. 2853–2862, 2016.

[21] I. Song, J. Lee, C. Byeon, S. Cho, H. Kim, I. Oh, and C. Park, "60ghz double-balanced drain-pumped up-conversion mixer using 90nm cmos," in *2013 IEEE MTT-S International Microwave Symposium Digest (MTT)*, 2013, pp. 1–4.

[22] S. Shiba, M. Sato, H. Matsumura, T. Takahashi, T. Suzuki, Y. Nakasha, and N. Hara, "An f-band fundamental mixer using 75-nm inp hemts for precise spectrum analysis," in *2013 European Microwave Integrated Circuit Conference*, 2013, pp. 137–140.

[23] H.-Y. Yang, J.-H. Tsai, T.-W. Huang, and H. Wang, "Analysis of a new 33–58-ghz doubly balanced drain mixer in 90-nm cmos technology," *IEEE Transactions on Microwave Theory and Techniques*, vol. 60, no. 4, pp. 1057–1068, 2012.

[24] H.-Y. Yang, J.-H. Tsai, C.-H. Wang, C.-S. Lin, W.-H. Lin, K.-Y. Lin, T.-W. Huang, and H. Wang, "Design and analysis of a 0.8–77.5-ghz ultra-broadband distributed drain mixer using 0.13-μm cmos technology," *IEEE Transactions on Microwave Theory and Techniques*, vol. 57, no. 3, pp. 562–572, 2009.

[25] S. E. Gunnarsson, N. Wadefalk, I. Angelov, H. Zirath, I. Kallfass, and A. Leuther, "A g-band (140 - 220 ghz) microstrip mmic mixer operating in both resistive and drain-pumped mode," in *2008 IEEE MTT-S International Microwave Symposium Digest*, 2008, pp. 407–410.

[26] F. Ellinger, L. Rodoni, G. Sialm, C. Kromer, G. von Buren, M. Schmatz, C. Menolfi, T. Toifl, T. Morf, M. Kossel, and H. Jackel, "30-40-ghz drain-pumped passive-mixer mmic fabricated on vlsi soi cmos technology," *IEEE Transactions on Microwave Theory and Techniques*, vol. 52, no. 5, pp. 1382–1391, 2004.

[27] L. de la Fuente, J. Portilla, and E. Artal, "Low noise ku-band drain mixer using p-hemt technology," in *1998 IEEE International Conference on Electronics, Circuits and Systems. Surfing the Waves of Science and Technology (Cat. No.98EX196)*, vol. 1, 1998, pp. 175–178 vol.1.

[28] M. Joao Rosario, R. Vitor Pedro, and J. Costa Freire, "Mesfet drain mixers: analysis and design," in *Proceedings. Electrotechnical Conference Integrating Research, Industry and Education in Energy and Communication Engineering',*, 1989, pp. 343–346.

[29] I. Kallfass, G. Eren, R. Weber, S. Wagner, D. Schwantuschke, R. Quay, and O. Ambacher, "High linearity active gan-hemt down-converter mmic for e-band radar applications," in *2014 9th European Microwave Integrated Circuit Conference*, 2014, pp. 128–131.

[30] Y. Zhu, O. P. Klimashov, B. Jin, F. G. Balteanu, S. Drogi, D. C. Bartle, and P. T. Dicarlo, "Analysis, simulation, and measurement of envelope tracking linearization," in *2016 Asia-Pacific Microwave Conference (APMC)*, 2016, pp. 1–4.

[31] J. C. Pedro and N. B. Carvalho, *Intermodulation distortion in microwave and wireless circuits*. Artech House, 2003.

[32] J. Pedro and J. Perez, "Accurate simulation of gaas mesfet's intermodulation distortion using a new drain-source current model," *IEEE Trans. on Microw. Theory and Tech.*, vol. 42, no. 1, pp. 25–33, 1994.

[33] L. Pagnini, G. Collodi, and A. Cidronali, "Analysis of a single-ended gan-based drain-pumped mixer for radar applications," in *Proceedings of SIE 2022*, G. Cocorullo, F. Crupi, and E. Limiti, Eds. Cham: Springer Nature Switzerland, 2023, pp. 63–68.

[34] ——, "A gan-hemt active drain-pumped mixer for s-band fmcw radar front-end applications," *Sensors*, vol. 23, no. 9, 2023. [Online]. Available: https://www.mdpi.com/1424-8220/23/9/4479

[35] S. Maas, "A gaas mesfet mixer with very low intermodulation," *IEEE Transactions on Microwave Theory and Techniques*, vol. 35, no. 4, pp. 425–429, 1987.

[36] N. Rojhani, M. Passafiume, M. Lucarelli, G. Collodi, and A. Cidronali, "Assessment of compressive sensing 2×2 mimo antenna design for millimeter-wave radar image enhancement," *Electronics*, vol. 9, no. 4, p. 624, 2020.

[37] M. Hefnawi, J. Bray, J. Bathurst, and Y. Antar, "Mimo radar using a vector network analyzer," *Electronics*, vol. 8, no. 12, 2019. [Online]. Available: https://www.mdpi.com/2079-9292/8/12/1447

[38] D. Li, Q. Xia, J. Huang, J. Li, H. Chang, B. Sun, and H. Liu, "A 24 ghz direct conversion receiver for fmcw ranging radar based on low flicker noise mixer," *Electronics*, vol. 10, no. 6, 2021. [Online]. Available: https://www.mdpi.com/2079-9292/10/6/722

[39] M. Passafiume, N. Rojhani, G. Collodi, and A. Cidronali, "Modeling small uav micro-doppler signature using millimeter-wave fmcw radar," *Electronics*, vol. 10, no. 6, p. 747, 2021.

[40] Y. Jiang, X. Lan, J. Shi, Z. Han, and X. Wang, "Multi-target parameter estimation of the fmcw-mimo radar based on the pseudo-noise

resampling method," *Sensors*, vol. 22, no. 24, 2022. [Online]. Available: https://www.mdpi.com/1424-8220/22/24/9706

[41] S. Fortunati, L. Sanguinetti, F. Gini, M. S. Greco, and B. Himed, "Massive mimo radar for target detection," *IEEE Transactions on Signal Processing*, vol. 68, pp. 859–871, 2020.

[42] M. Passafiume, G. Collodi, and A. Cidronali, "Design principles of batteryless transponder for vehicular dsrc at 5.8 ghz," *IEEE Journal of Radio Frequency Identification*, vol. 4, no. 4, pp. 491–505, 2020.

[43] A. Cidronali, S. Maddio, G. Collodi, and G. Manes, "Design trade-off for a compact 5.8 ghz dsrc transponder front-end," *Microwave and Optical Technology Letters*, vol. 57, no. 5, pp. 1187–1191, 2015.

[44] A. Cidronali, L. Pagnini, G. Collodi, and M. Passafiume, "A highly linear ka-band gan-on-si active balanced mixer for radar applications," *IEEE Transactions on Circuits and Systems I: Regular Papers*, vol. 69, no. 11, pp. 4453–4464, 2022.

[45] S. Pruvost, I. Telliez, F. Danneville, G. Dambrine, N. Rolland, and F. Pourchon, "A 40 ghz single-ended down-conversion mixer in 0.13 μm sigec bicmos hbt," *IEEE Microwave and Wireless Components Letters*, vol. 15, no. 8, pp. 496–498, 2005.

[46] P. Panwar, N. Pandit, and N. P. Pathak, "Design, analysis and characterization of active hbt down conversion rf mixer for wlan applications," in *2017 IEEE International Conference on Antenna Innovations & Modern Technologies for Ground, Aircraft and Satellite Applications (iAIM)*, 2017, pp. 1–6.

[47] J. M. Salem and D. S. Ha, "A high temperature active gan-hemt downconversion mixer for downhole communications," in *2016 IEEE International Symposium on Circuits and Systems (ISCAS)*, 2016, pp. 946–949.

[48] S. Schafer and Z. Popović, "Multi-frequency measurements for supply modulated transmitters," *IEEE Transactions on Microwave Theory and Techniques*, vol. 63, no. 9, pp. 2931–2941, 2015.

[49] R. Joao and F. Costa, "Design technique for mesfet mixers for maximum conversion gain," *IEEE Transactions on Microwave Theory and Techniques*, vol. 38, no. 12, pp. 1972–1979, 1990.

[50] H. Lee and S. Jeon, "A gaas p-hemt distributed drain mixer with low lo drive power, high isolation, and zero power consumption," *IEEE Access*, vol. 9, pp. 158 420–158 425, 2021.

[51] J. Kim, "A wideband and low-power distributed cascode mixer using inductive feedback," *Sensors*, vol. 22, no. 22, 2022. [Online]. Available: https://www.mdpi.com/1424-8220/22/22/9022

[52] E. A. Ball, "Investigation into the relationship between conversion gain, local oscillator drive level and dc bias in a sige transistor transconductance modulated mixer at 24-28 ghz," in *2021 IEEE Texas Symposium on Wireless and Microwave Circuits and Systems (WMCS)*, 2021, pp. 1–6.

[53] ——, "Predicting the performance of a 26 ghz transconductance modulated downconversion mixer as a function of lo drive and dc bias," *Electronics*, vol. 11, no. 16, 2022. [Online]. Available: https://www.mdpi.com/2079-9292/11/16/2516

[54] S. Peng, P. J. McCleer, and G. I. Haddad, "Nonlinear models for the intermodulation analysis of fet mixers," *IEEE transactions on microwave theory and techniques*, vol. 43, no. 5, pp. 1037–1045, 1995.

[55] J. Garcia, M. De la Fuente, J. Pedro, N. Carvalho, Y. Newport, A. Mediavilla, and A. Tazon, "Time-varying volterra-series analysis of spectral regrowth and noise power ratio in fet mixers," *IEEE Trans. on Microw. Theory and Tech.*, vol. 49, no. 3, pp. 545–549, 2001.

[56] M. Mollaalipour and H. Miar-Naimi, "An improved high linearity active cmos mixer: Design and volterra series analysis," *IEEE Transactions on Circuits and Systems I: Regular Papers*, vol. 60, no. 8, pp. 2092–2103, 2013.

[57] L. Pagnini, G. Collodi, and A. Cidronali, "A mixer-like nonlinear analysis for gan hemt supply-modulated power amplifier at 3.8 ghz," in *2022 17th European Microwave Integrated Circuits Conference (EuMIC)*, 2022, pp. 9–12.

[58] L. Pagnini, G. Collodi, M. Passafiume, and A. Cidronali, "A new architecture of broadband gaas mmic balanced mixer for very high rf/if isolation for 0.5-18.5 ghz signal analysis," in *2022 17th European Microwave Integrated Circuits Conference (EuMIC)*, 2022, pp. 216–219.

[59] S. Maas and A. Crosmun, "Modeling the gate i/v characteristic of a gaas mesfet for volterra-series analysis," *IEEE Trans. on Microw. Theory and Tech.*, vol. 37, no. 7, pp. 1134–1136, 1989.

[60] *6-W RF Power GaN HEMT*, Wolfspeed, 2022, rev. 3.4. [Online]. Available: https://assets.wolfspeed.com/uploads/2020/12/CGH40006S.pdf

[61] C. Florian, T. Cappello, A. Santarelli, D. Niessen, F. Filicori, and Z. Popović, "A prepulsing technique for the characterization of gan power amplifiers with dynamic supply under controlled thermal and trapping states," *IEEE Transactions on Microwave Theory and Techniques*, vol. 65, no. 12, pp. 5046–5062, 2017.

[62] K. Kellogg, S. Khandelwal, L. Dunleavy, and J. Wang, "Characterization of thermal and trapping time constants in a gan hemt," in *2020 94th ARFTG Microwave Measurement Symposium (ARFTG)*, 2020, pp. 1–4.

[63] G. P. Gibiino, C. Florian, A. Santarelli, T. Cappello, and Z. Popović, "Isotrap pulsed *iv* characterization of gan hemts for pa design," *IEEE Microwave and Wireless Components Letters*, vol. 28, no. 8, pp. 672–674, 2018.

[64] C. Florian, G. P. Gibiino, and A. Santarelli, "Characterization and modeling of rf gan switches accounting for trap-induced degradation under operating regimes," *IEEE Transactions on Microwave Theory and Techniques*, vol. 66, no. 12, pp. 5491–5500, 2018.

[65] T. Cappello, C. Florian, A. Santarelli, and Z. Popovic, "Linearization of a 500-w l-band gan doherty power amplifier by dual-pulse trap characterization," in *2019 IEEE MTT-S International Microwave Symposium (IMS)*, 2019, pp. 905–908.

[66] A. M. Angelotti, G. P. Gibiino, C. Florian, and A. Santarelli, "Trapping dynamics in gan hemts for millimeter-wave applications: Measurement-based characterization and technology comparison," *Electronics*, vol. 10, no. 2, 2021. [Online]. Available: https://www.mdpi.com/2079-9292/10/2/137

[67] E. A. Ball, "Investigation into the relationship between conversion gain, local oscillator drive level and dc bias in a sige transistor transconductance modulated mixer at 24-28 ghz," in *2021 IEEE Texas Symposium on Wireless and Microwave Circuits and Systems (WMCS)*, 2021, pp. 1–6.

[68] J. A. Garcia, J. C. Pedro, M. L. De La Fuente, N. B. De Carvalho, A. M. Sánchez, and A. T. Puente, "Resistive fet mixer conversion loss and imd optimization by selective drain bias," *IEEE Trans. on Microw. Theory and Tech.*, vol. 47, no. 12, pp. 2382–2392, 1999.

[69] J. A. Garcia, M. L. De la Fuente, J. M. Zamanillo, A. Mediavilla, A. Tazon, J. C. Pedro, and N. B. Carvalho, "Intermodulation distortion analysis of fet mixers under multitone excitation," in *2000 30th European Microwave Conference*, 2000, pp. 1–4.

[70] A. Cidronali, K. Gupta, J. Jargon, K. Remley, D. DeGroot, and G. Manes, "Extraction of conversion matrices for p-hemts based on vectorial large-signal measurements," in *IEEE MTT-S International Microwave Symposium Digest, 2003*, vol. 2.   IEEE, 2003, pp. 777–780.

[71] N. Weerathunge, S. Chakraborty, S. J. Mahon, G. McCulloch, A. Jones, and M. Heimlich, "Design of a q-band single-balanced passive mixer in 0.15μm gan technology," in *2021 IEEE Asia-Pacific Microwave Conference (APMC)*, Nov 2021, pp. 232–234.

[72] I. Kallfass, G. Eren, R. Weber, S. Wagner, D. Schwantuschke, R. Quay, and O. Ambacher, "High linearity active GaN-hemt down-converter mmic for e-band radar applications," in *2014 9th European Microwave Integrated Circuit Conference*.   IEEE, 2014, pp. 128–131.

[73] S. Liu, J. Xu, B. Zhang, and Z. Xu, "A double-balanced down converter mixer in GaN-on-Si hemt technology," in *2014 IEEE International Conference on Communiction Problem-solving*. IEEE, 2014, pp. 550–552.

[74] T. Chang, W. Wu, J. Lin, S. Jang, F. Ren, S. Pearton, R. Fitch, and J. Gillespie, "Analysis and design of alGaN/GaN hemt resistive mixers," *Microwave and Optical Technology Letters*, vol. 49, no. 5, pp. 1152–1154, 2007. [Online]. Available: https://onlinelibrary.wiley.com/doi/abs/10.1002/mop.22390

[75] C.-S. Yeh, H.-L. Kao, J.-Y. Ke, B.-W. Wang, C.-L. Cho, H.-C. Chiu, and L.-C. Chang, "A 3.5 GHz antiparallel diode pair mixer in GaN-on-Si hemt technology," in *2012 4th International High Speed Intelligent Communication Forum*, 2012, pp. 1–4.

[76] V. Di Giacomo, N. Thouvenin, C. Gaquiere, A. Santarelli, and F. Filicori, "Modelling and design of a wideband 6 - 18 GHz GaN resistive mixer," in *2009 European Microwave Integrated Circuits Conference (EuMIC)*, 2009, pp. 459–462.

[77] M. Sudow, K. Andersson, M. Fagerlind, M. Thorsell, P.-A. Nilsson, and N. Rorsman, "A single-ended resistive x-band alGaN/GaN hemt mmic mixer," *IEEE Trans. on Microw. Theory and Tech.*, vol. 56, no. 10, pp. 2201–2206, 2008.

[78] M. San-Miguel-Montesdeoca, S. Mateos-Angulo, D. Mayor-Duarte, D. Ramos-Valido, S. L. Khemchandani, and J. del Pino, "A GaN-on-Si passive upconversion mixer for ku-band applications," *AEU - International Journal of Electronics and Communications*, vol. 124, p. 153358, 2020. [Online]. Available: https://www.sciencedirect.com/science/article/pii/S1434841120305987

[79] J. Kang, A. Kurdoghlian, A. Margomenos, H. Moyer, D. Brown, and C. Mcguire, "Ultra-wideband, high-dynamic range, low loss GaN hemt mixer," *Electronics Letters*, vol. 50, pp. 295–297, 02 2014.

[80] A. K. Kwan, M. Younes, O. Hammi, M. Helaoui, and F. M. Ghannouchi, "Linearization of a highly nonlinear envelope tracking power amplifier targeting maximum efficiency," *IEEE Microwave and Wireless Components Letters*, vol. 27, no. 1, pp. 82–84, 2017.

[81] W.-Y. Kim, H. S. Son, J. H. Kim, J. Y. Jang, I. Y. Oh, and C. S. Park, "A cmos envelope-tracking transmitter with an on-chip common-gate voltage modulation linearizer," *IEEE Microwave and Wireless Components Letters*, vol. 24, no. 6, pp. 406–408, 2014.

[82] J.-L. Woo, S. Park, and Y. Kwon, "A wideband envelope-tracking cmos linear transmitter without digital predistortion," in *2015 IEEE Radio Frequency Integrated Circuits Symposium (RFIC)*, 2015, pp. 367–370.

[83] S. Jin, K. Moon, B. Park, J. Kim, Y. Cho, H. Jin, D. Kim, M. Kwon, and B. Kim, "Cmos saturated power amplifier with dynamic auxiliary circuits for optimized envelope tracking," *IEEE Transactions on Microwave Theory and Techniques*, vol. 62, no. 12, pp. 3425–3435, 2014.

[84] A. Cidronali, G. Manes, N. Giovannelli, T. Vlasits, and R. Hernaman, "Efficiency and linearity enhancements with envelope shaping control in dual-band envelope tracking gaas pa," in *2011 6th European Microwave Integrated Circuit Conference*, 2011, pp. 308–311.

[85] A. Cidronali, S. Maddio, G. Collodi, and G. Manes, "Envelope tracking pa x-parameters characterization for transceivers system level analysis," in *2014 44th European Microwave Conference*, 2014, pp. 1440–1443.

[86] D. Kim, D. Kang, J. Choi, J. Kim, Y. Cho, and B. Kim, "Optimization for envelope shaped operation of envelope tracking power amplifier," *IEEE Transactions on Microwave Theory and Techniques*, vol. 59, no. 7, pp. 1787–1795, 2011.

[87] G. Casini, A. Cidronali, and G. Manes, "Investigation of x-parameters modeling for accurate envelope tracking power amplifier system simulations," in *2013 IEEE MTT-S International Microwave Symposium Digest (MTT)*, 2013, pp. 1–4.

[88] G. P. Gibiino, G. Avolio, D. Schreurs, A. Santarelli, and F. Filicori, "Mixer-like modeling with dynamic baseband characterization for supply-modulated pas," in *2014 44th European Microwave Conference*, 2014, pp. 1313–1316.

[89] L. Pagnini, G. Collodi, M. Passafiume, and A. Cidronali, "A new architecture of broadband gaas mmic balanced mixer for very high rf/if isolation for 0.5-18.5 ghz signal analysis," in *2022 17th European Microwave Integrated Circuits Conference (EuMIC)*, 2022, pp. 216–219.

[90] S. A. Maas, "Microwave mixers," *Norwood*, 1986.

[91] A. Cidronali, "Local oscillator phase-dependent linearized mixer modeling based on large-signal vector measurements," *IEEE Transactions on Microwave Theory and Techniques*, vol. 66, no. 1, pp. 81–90, 2017.

[92] A. Cidronali, C. Accillaro, and G. Manes, "Mildly nonquasi-static two-port device model extraction by integrating linearized large-signal vector measurements," *IEEE transactions on microwave theory and techniques*, vol. 55, no. 11, pp. 2277–2289, 2007.